RESEARCH ARTICLE

Characterizing lithological, weathering, and hydrothermal alteration influences on volcanic rock properties via spectroscopy and laboratory testing: a case study of Mount Ruapehu volcano, New Zealand

Lauren N. Schaefer[1,2] · Gabor Kereszturi[3] · Ben M. Kennedy[1] · Marlène Villeneuve[4]

Abstract

The geomechanical characterization of volcanic material has important implications for geothermal and mineral exploration, engineering design, geophysical signals of volcano unrest, and models of instability and mass flows. Chemical weathering and hydrothermal systems can alter the host rock, leading to changes in mechanical behavior and failure mode. Here, we compare the physical and mechanical properties of lava, autoclastic breccia, and pyroclastic (scoria) rocks from Mount Ruapehu volcano (Ruapehu) in New Zealand to mineralogical composition determined via infrared spectroscopy and scanning electron microscopy (SEM) with energy-dispersive X-ray spectroscopy (EDS). We use correlation matrices, principal component analysis, and parametric analysis to determine which parameters can be used to predict physical and mechanical properties and form the basis for transfer functions. Laboratory-based spectroscopy shows that the samples contain absorption features indicative of Al- and Mg-rich hydrous phyllosilicates (e.g., kaolinite, halloysite, montmorillonite), Fe- oxides (e.g., goethite), and sulfates attributed to surface weathering, supergene, and steam-heated alteration. We find that porosity and primary lithology are the predominant control on physical and mechanical properties, followed by the pervasiveness of weathering/alteration, and then mineralogical composition. Several properties, such as porosity, uniaxial compressive strength, P-wave seismic velocity, density, and Young's modulus, show strong correlations with other properties, indicating the potential for transfer functions between these properties. Hydrothermally altered rocks near the vent complex (up to ~ 400 m depth beneath the crater lake) with high-intensity hydrothermal alteration do not follow typical physical and mechanical property trends due to high clay content, low permeability, and low strength. The presence of these rocks within the edifice at Ruapehu implies local barriers to fluid flow and subsequent pore pressure variations. Additionally, they may have less than half the strength than would be dictated by typical porosity-strength trends for surface rocks, increasing the likelihood of structural failure. Trends in the pervasiveness of weathering with physical and mechanical properties, along with shifts in the position of spectral absorption peaks as hydrothermal/weathering alteration increases, suggest that it may be possible to extrapolate properties from imaging spectroscopy.

Keywords Rock mechanics · Spectral imaging · Hoek–Brown · Andesite · Failure mode · Argillic alteration

✉ Lauren N. Schaefer
lschaefer@usgs.gov

1 Earth and Environment, University of Canterbury, Private Bag 4800, Christchurch, New Zealand

2 Now at: U.S. Geological Survey, Geologic Hazards Science Center, 1711 Illinois St, Golden, CO 80401, USA

3 Volcanic Risk Solutions, School of Agriculture and Environment, Massey University, Private Bag 11 222, Palmerston North, New Zealand

4 Subsurface Engineering, Montanuniversität Leoben, Franz Josef Strasse 18, Leoben, Austria

Introduction

Chemical weathering and hydrothermal alteration influence the physical and mechanical properties of volcanic rock, with implications for geothermal and epithermal mineral resources (Heap et al. 2019a), the use of volcanic material in the construction industry (Yildiz et al. 2010), failure modes and the evolution of rock physical properties (Heap et al. 2015c), and volcano structural stability (Watters et al. 2000). In active volcanic environments, rock properties are critical for modeling instability or mass flows, and interpreting geophysical signals of volcano unrest (e.g., volcano-seismic

or geodetic; Reid et al. 2001; Mordensky et al. 2019a; Heap et al. 2020; Hickey et al. 2020). Inherent heterogeneities in volcanic primary material create physically and mechanically varied structures (Mordensky et al. 2018; Saubin et al. 2019). These heterogeneities are exacerbated by the circulation of hydrothermal fluids and chemical weathering under widely varying temperature (surface temperature to > 400 °C), chemical, temporal, and spatial conditions. These processes result in mineral oxidation, dissolution, replacement, and/or precipitation that variably alter the physical and mechanical properties of the volcanic host rock (e.g., Reid et al. 2001; Dobson et al. 2003; Ball et al. 2013; Siratovich et al. 2014; Wyering et al. 2014; Mordensky et al. 2018, 2019a, 2019b; Farquharson et al. 2019; Heap et al. 2019a, 2019b; Kennedy et al. 2020). For example, weathering and alteration can decrease or increase porosity and permeability of volcanic rock depending on the nature of the host rock, the fluid type and composition, temperature, and the duration and manner of rock-fluid interaction (Frolova et al. 2015; Farquharson et al. 2019; Mordensky et al. 2019b; Villeneuve et al. 2020). Changes in these properties in turn influence fluid flow, strength, and the deformation response of rock masses (Mordensky et al. 2022). A considerable presence of clays due to hydrothermal alteration has been attributed to large-scale volcano collapses (López and Williams 1993; Crowley and Zimbelman 1997), supported by numerical simulations of collapse scenarios (Reid et al. 2001; Ball et al. 2018).

Here, we explore the influence of weathering and hydrothermal alteration on the physical and mechanical properties of lava, autoclastic breccia, and pyroclastic (scoria) rocks from Mount Ruapehu (Ruapehu), an active andesitic stratovolcano in New Zealand. Ruapehu is a glaciated volcano with both active and relict hydrothermal systems with variable surface exposure (Kereszturi et al. 2020; Douglas et al. 2022), resulting in a variety of fresh, weathered, and hydrothermally altered material (Townsend et al. 2017). Rock alteration mineralogy is determined using a combination of infrared spectroscopy and scanning electron microscopy (SEM) with energy-dispersive X-ray spectroscopy (EDS). Infrared spectroscopy collects information from hundreds of narrow and contiguous spectral bands in the visible (400–700 nm), near-infrared (NIR; 700–1000 nm) and shortwave infrared (SWIR; 1000–2500 nm) wavelengths, capable of identifying chemical characteristics of materials using indicator minerals with characteristic absorption features (van der Meer 2018). Many indicator minerals are common weathering, oxidation, and hydrothermal alteration products in volcanic environments. For example, iron is highlighted in the NIR region, useful for detecting minerals such as goethite, hematite, and jarosite (Zimbelman et al. 2005). Al-, Fe-, Mg-, -OH, -SO_4, -CO_3 and -H_2O-bearing minerals can be detected in the SWIR region, identifying

minerals such as alunite, gypsum, anhydrite, topaz, muscovite, biotite, epidote, calcite, dolomite, and clay minerals (Hunt and Ashley 1979; Swayze et al. 2014; Neal et al. 2018). Infrared spectroscopy can also be sensitive to other mechanically relevant rock microstructure properties such as grain size and crystallinity (Clarke 1999; Ruitenbeek et al. 2019; Okada et al. 2020).

The aims of this paper are to: (1) produce a spectroscopic and petrologic description of the fresh, weathered, and hydrothermally altered rock of Ruapehu volcano, (2) physically and mechanically characterize these rocks, and (3) examine the relationships between physical and mechanical properties and the type and extent of weathering and hydrothermal alteration. Mineralogical-physical–mechanical relationships will help to develop geotechnical models of volcanic and hydrothermal systems and guide numerical simulations of volcanic hazards.

Materials and methods

Study area and materials

Ruapehu is a complex andesitic composite volcano located in the Taupo Volcanic Zone of the central North Island of New Zealand (Fig. 1). The volcano is frequently active, with several historic small-to-moderate explosive eruptions and lahar events (Scott 2013). The oldest geologic rocks are dated at 250 ky and were exposed to glaciation up until 10 ky (Hackett 1985), and the youngest fresh magmatic rocks were erupted in 1996 (Nakagawa et al. 1999). The stratigraphic framework of Ruapehu comprises four formations, based on geochronology, geochemistry and stratigraphic relationships, pinpointing distinct spatial–temporal stages of volcano evolution (Fig. 1): Te Herenga (200 to 150 ka), Wahianoa (166–80 ka), Mangawhero (50–15 ka) and Whakapapa (< 15 ka) formations (Hackett and Houghton 1989; Price et al. 2012; Conway et al. 2016; Townsend et al. 2017; Fig. 1c). The volcano has an active hydrothermal system underneath the summit vent that hosts a crater lake (Christenson and Wood 1993; Christenson et al. 2010). Mineral assemblages of ejecta indicate local temperatures greater than 750 °C, reflecting vapor phase or contact metamorphism within the vent associated with high-level magma emplacement (Christenson and Wood 1993). A physical model of the vent system from Christenson and Wood (1993) describes a deeper central vent complex with a northern-inclined vent offshoot originating around 350 m below the Crater Lake. Fossil hydrothermal systems are also variably exposed at the surface around the summit plateau (see areas of argillic alteration outside of the currently active Crater Lake area, Fig. 1b; Kereszturi et al. 2020; Douglas et al. 2022). This varied geological, glacial, and hydrothermal

Fig. 1 Location and variability of samples with respect to spectral properties and geological formations. (**a**) Topographic map. (**b**) Simplified geological map, with the major geological formations (after Townsend et al. 2017). (**c**) Alteration map of the summit plateau based on airborne hyperspectral imagery from Kereszturi et al. (2020). Note not all sample locations are included in this zoomed view of the summit plateau
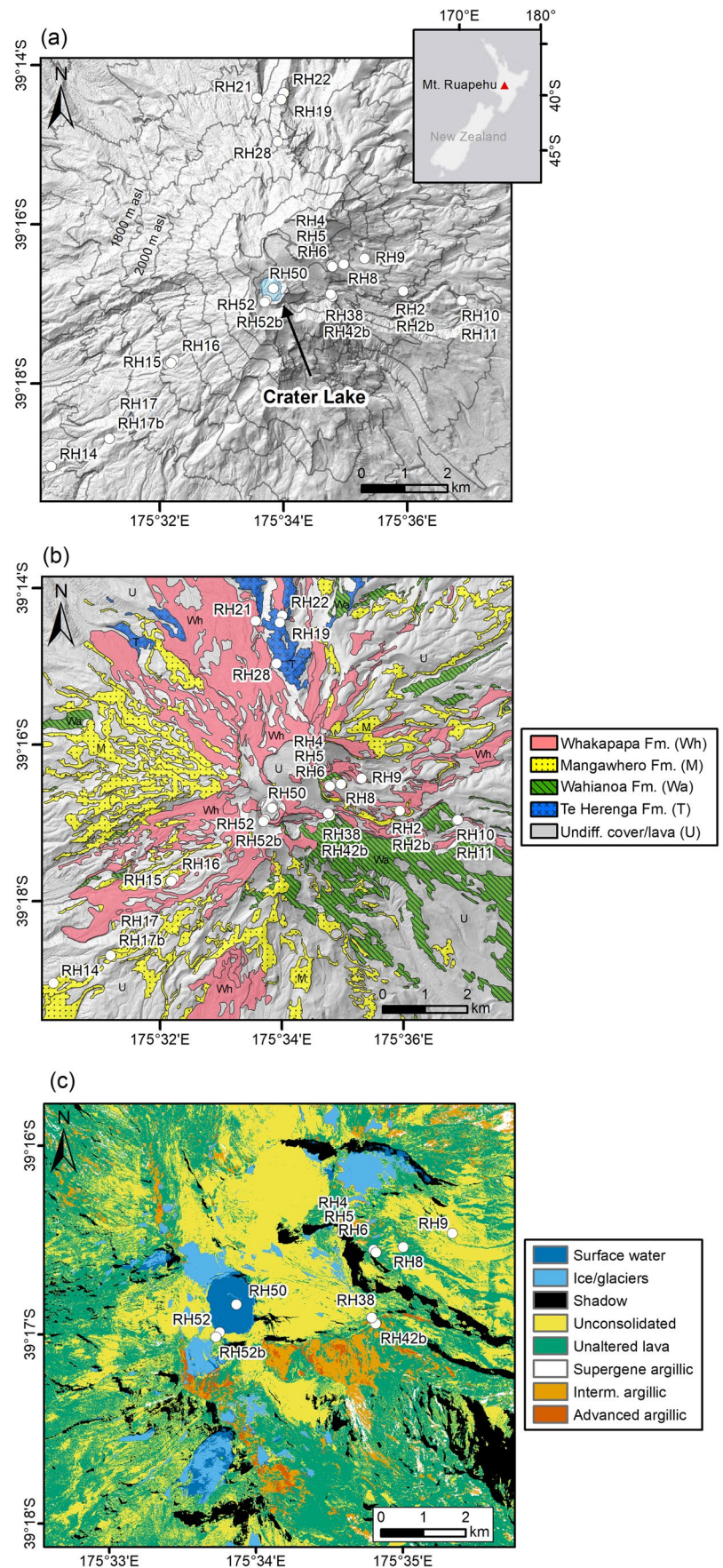
history results in a wide variety of fresh, weathered, and altered material.

Sampling locations were partially directed by aerial hyperspectral imagery collected using a push-broom, VNIR-SWIR AISAFenix imaging system, flown in March of 2018 (Kereszturi et al. 2020; Miller et al. 2020; Fig. 1b). A total of 23 blocks of lava, autoclastic breccia, and pyroclastic (scoria) rocks varying from fresh to pervasively altered were selected to represent the variability of the physical properties of the material forming the volcanic edifice (Fig. 1, Fig. 2, Table 1). The blocks had a volume of c. 8000 cm^3 (typical edge length of 20 cm) and were large enough to obtain all the test specimens of a given rock type from the same piece. Each block was inspected for macroscopic defects so that it would provide test specimens free from fractures, seams, partings, or joints. Block sample names follow the same nomenclature as (Kereszturi et al. 2020). All blocks are considered surface samples excluding RH50; RH50 is a ballistic block from the 1995–1996 eruption, composed of moderately to highly altered andesites with pores and vesicles rarely filled with elemental sulfur and associated anhydrite, pyrite, and natroalunite (Christenson et al. 2010). During this eruption, the introduction of gas/fluid at depth promoted catastrophic failure of a partial mineralogic seal

developed at the top of the hydrothermal systems in the northward-inclined vent beneath Crater Lake (Kilgour et al. 2010). Estimates of penetration depth into the vent complex indicate depths between 275 and 410 m, and the formerly molten elemental sulfur indicates a minimum pre-eruption temperature in the source area of 119 °C (Christenson et al. 2010). Thus, the sample originated within the current vent complex (Christenson and Wood 1993), and is considered a subsurface sample. Pyroclastic sample RH15 is a block of scoria located in an undifferentiated tephra fall deposit. The term 'sample' refers to the 23 rock blocks, while cores or pieces from each block are referred to as 'specimens' throughout.

Laboratory spectroscopy and Scanning Electron Microscopy (SEM)

Each of the 23 blocks listed in Table 1 was measured using an ASD FieldSpec® 4 Hi-Res NG spectroradiometer, which recorded 2151 spectral bands between 350 and 2500 nm. This instrument has a full-width-half-maximum (FWHM) of 3 nm at 700 nm and 8 nm at 1400–2100 nm regions. The spectral bandwidth is 1.4 nm between 350–1000 nm, as well as 1.1 nm between 1001 and 2500 nm. Spectral data

Fig. 2 Photographs of the samples and porosity as determined by helium pycnometer

increasing porosity →

20 mm

sample =	RH17b	RH52	RH50	RH2b	RH5	RH17	RH10
porosity =	1.57%	2.84%	3.64%	5.59%	6.07%	6.32%	6.59%

RH21	RH16	RH9	RH11	RH14	RH2	RH52b	RH8
6.77%	8.59%	9.14%	9.44%	9.44%	14.70%	17.38%	19.45%

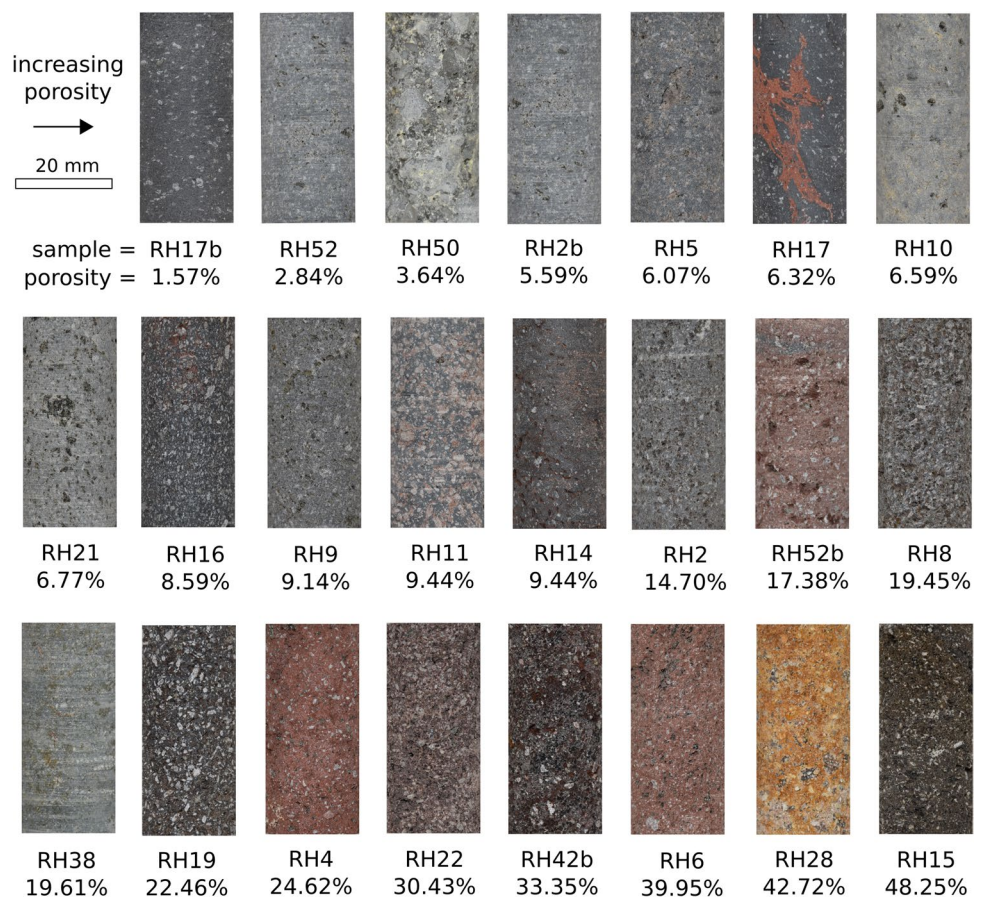| RH38	RH19	RH4	RH22	RH42b	RH6	RH28	RH15
19.61%	22.46%	24.62%	30.43%	33.35%	39.95%	42.72%	48.25%

Table 1 Location, geologic formation, and geologic member of samples used in this study. A description of the formations and members can be found in (Townsend et al. 2017). Undiff = undifferentiated

No	Block	Location	UTM east	UTM North	Formation	Member
1	RH2	Tukino	379236.35	5651000.505	Mangawhero	Horonuku
2	RH2b	Tukino	379236.348	5651000.505	Mangawhero	Horonuku
3	RH4	Tukino	377566.725	5651595.04	Whakapapa	Iwikau
4	RH5	Tukino	377562.617	5651602.295	Whakapapa	Iwikau
5	RH6	Tukino	377585.291	5651575.887	Whakapapa	Iwikau
6	RH8	Tukino	377853.391	5651625.957	Mangawhero	Horonuku
7	RH9	Tukino	378333.061	5651763.1	Whakapapa	Iwikau
8	RH10	Tukino	380579.028	5650771.933	Wahianoa	Wahinoa undiff
9	RH11	Tukino	380602.148	5650782.097	Wahianoa	Wahinoa undiff
10	RH14	Turoa	371062.95	5646926.922	Mangawhero	Makotuku
11	RH15	Turoa	373905.69	5649405.62	Late Quaternary tephra	Late Quaternary undiff
12	RH16	Turoa	373838.715	5649332.308	Mangawhero	Waitonga
13	RH17	Turoa	372410.371	5647578.841	Mangawhero	Makotuku
14	RH17b	Turoa	372410.371	5647578.841	Mangawhero	Makotuku
15	RH19	Whakapapa	375835.142	5655487.917	Whakapapa	Iwikau
16	RH21	Whakapapa	376462.298	5655607.92	Te Herenga	Te Herenga undiff
17	RH22	Whakapapa	376402.264	5655448.213	Te Herenga	Te Herenga undiff
18	RH28	Whakapapa	376323.48	5654474.1	Te Herenga	Te Herenga undiff
19	RH38	Tukino	377584.94	5650878.81	Wahianoa Fmt	Wahinoa undiff
20	RH42b	Tukino	377544.95	5650936.57	Whakapapa	Crater Lake
21	RH50	--	--	--	--	95/96 ejecta
22	RH52	Crater lake	376056.549	5650793.094	Whakapapa	Crater Lake
23	RH52b	Crater lake	376019.243	5650747.056	Whakapapa	Crater Lake

were captured using a High Brightness contact probe with a halogen light illumination source. The contact probe has a measurement spot size of 10 mm. Each measurement was calibrated using a white Spectralon® Diffuse Reflectance Standard. Both freshly chipped surfaces (sample interior) and the exterior of the sample were measured for a total of 3–5 spectral readings per block. Phenocrysts are typically 1 mm or smaller (Fig. 3); therefore, the contact probe size, being 10 times larger than the average phenocryst size, was sufficient to capture the spatial heterogeneity in each block. See Danner et al. (2015) for FieldSpec schematic and spectral sampling details.

Inherent variation in detector sensitivity and variations in temperature conditions can cause spectral drift at two wavelength locations where detector arrays meet (e.g., VNIR and SWIR). These drifts were corrected by applying a splice correction function using the ASD ViewSpec Pro software (Danner et al. 2015). The splice correction function considers the average of tangents at either side of a break point to determine the new points through which the line passes without drift (see Danner et al. (2015) for schematic and details). The splice-corrected spectral readings for each block were then averaged. The spectral data were then normalized using a convex hull continuum removal method. The continuum is a convex "hull" of straight-line segments fitted over the top of the spectrum that connect local spectral maxima. The continuum is removed by dividing the original reflectance value by the corresponding values of the continuum line (convex hull) at a given wavelength. Removing this continuum standardizes isolated absorption features for comparison between samples (Kokaly and Clark 1999; Huang et al. 2004).

The sample mineralogy was further constrained using a ThermoFisher Scientific™ FEI Quanta 200 Environmental Scanning Electron Microscope (SEM) operated in Back-Scattered Electron (BSE) mode under accelerating voltage of 20 kV, with a working distance of 10 mm, at Massey University's Manawatu Imaging Centre. Minerals were recognized based on their textural and crystal habits as well as using Energy-dispersive X-ray Spectroscopy (EDS) (Shindo and Oikawa 2002; Severin 2004).

Laboratory physical and mechanical measurements

The 23 blocks were cored to create several specimens per block (5 to 8) with a diameter of 20 mm, and then ground to a length:diameter ratio of 2–2.15:1 (see Supplementary Table 1 for details of each specimen). For each specimen, we measured porosity, permeability, and compressional (Vp) and shear wave (Vs) velocity. Dynamic Young's modulus and dynamic Poisson's ratio were calculated from Vp and Vs results. Porosity, permeability, Vp, Vs,

Fig. 3 A (**a**) Continuum-removed spectral reflectance curves of typical alteration minerals in volcanic environments from non-altered (RH17) to pervasively altered (RH50)- see descriptions in Table 3. Note the spectral shift from 550 to 480 nm where hematite is being replaced by goethite as a surface weathering product. The curves are offset for clarity by 0.1 percent. Each spectral curve has a maximum reflectance value of '1', and the following minimum values: RH50=0.74, RH38=0.80, RH28=0.51, RH22=0.79, RH6=0.67, RH17=0.77. (**b-e**) Optical microscope and SEM images demonstrating textural and mineralogical changes through hydrothermal and weathering alterations. Labeled mineral phases: v – void/vugg, m – titanomagnetite, plg – plagioclase, opx – orthopyroxene, cpx – clinopyroxene, sm – smectites, kao – kaolinite, qtz – quartz, geo – goethite, py – pyrite, al – alunite, hem – hematite, s – sulfur
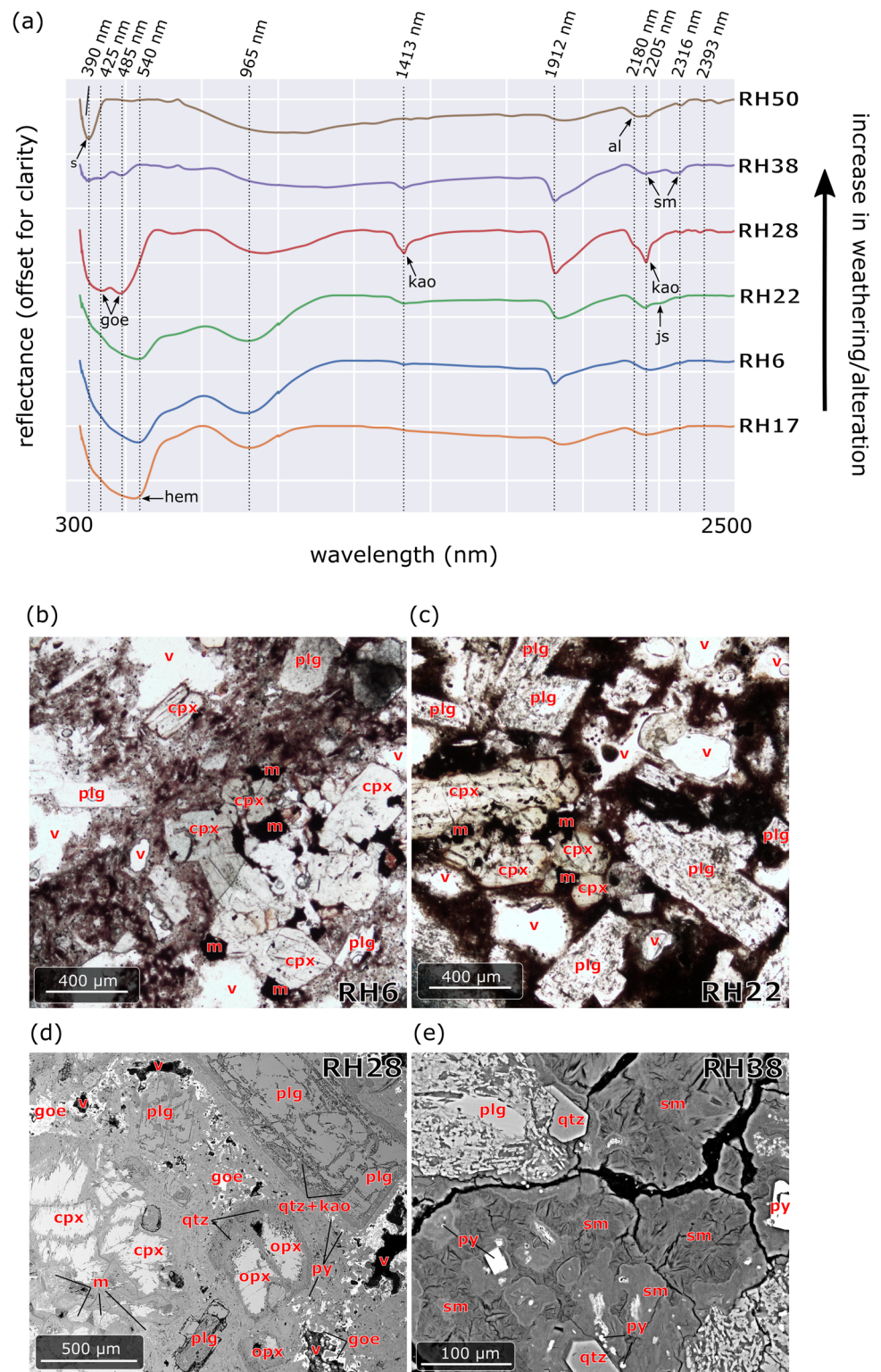
dynamic Young's modulus, and dynamic Poisson's ratio values were then averaged for each block. Magnetic susceptibility was measured on the natural face and a cut face of each block using a magnetic susceptibility meter and averaged to produce one value of magnetic susceptibility per block. Two to three specimens from each block were then used for uniaxial compressive strength (UCS) experiments, from which static Young's modulus values were calculated. UCS and static Young's modulus were also averaged to produce a single value for each block. Another

three specimens from each block were used for triaxial compressive strength testing. Triaxial results were used to calculate friction angle, cohesion, and the Hoek–Brown material constant for intact rock (m_i) for each block. All specimens were oven-dried at 60 °C for a minimum of 48 h and then allowed to cool to room temperature prior to testing.

All physical and mechanical property testing was conducted at the University of Canterbury rock mechanics laboratory. The physical and mechanical properties measured and examined in this study are commonly used to develop models of fluid flow (e.g., porosity, permeability; Day 1996; Gonnermann and Manga 2007; Kennedy et al. 2020), slope failure (e.g., UCS, friction angle, cohesion, material constant for intact rock m_i; Apuani et al. 2005; Schaefer et al. 2013; Heap et al. 2021; Wallace et al. 2021), subsurface imaging, and monitoring deformation and geophysical phenomena such as seismicity (e.g., Young's modulus, Poisson's ratio, Vp, Vs, density, magnetic susceptibility; Lu et al. 2005; Mordensky et al. 2019a; Heap et al. 2020).

Pearson's correlation coefficient (PCC or Pearson's *r*) and Spearman's rank correlation coefficient (*SCC* or Spearman's ρ) were used to correlate one physical or mechanical property (*X*) to another physical or mechanical property (*Y*). Pearson's correlation coefficient is the measure of the linear correlation between two variables as:

$$PCC(r)_{X,Y} = \frac{cov(X,Y)}{\sigma_X \sigma_Y} \tag{1}$$

where *cov* is the covariance, σ_X is the standard deviation of *X* and σ_Y is the standard deviation of *Y*. Spearman's rank correlation coefficient is the measure of the monotonic correlation between two variables. For a sample size of *n*, the *n* raw scores X_i and Y_i are converted to ranks $R(X_i)$ and $R(Y_i)$, and *SCC* is computed as:

$$SCC(\rho)_{R(X),R(Y)} = \frac{cov(R(X), R(Y))}{\sigma_{R(X)} \sigma_{R(Y)}} \tag{2}$$

where the *cov* is the covariance of the rank variable, and the $\sigma_{R(X)}$ and $\sigma_{R(Y)}$ are the standard deviation of the two rank variables being compared. The correlation coefficient values (*r* or ρ) range from -1 to 1, with '-1' indicating a total negative correlation between variables, '0' indicating no relationship, and '1' indicating a total positive relationship. The strength of the relationship has different interpretations among scientific research areas (see Akoglu 2018); our interpretations of the Pearson's and Spearman's correlation coefficients are as follows: $(-)0.10$ to $(-)0.39$ is a "weak" relationship, $(-)0.40$ to $(-)0.59$ is a "moderate" relationship, $(-)0.60$ to $(-)0.79$ is a "strong" relationship, and $(-)0.80$ to $(-)1.0$ is a "very strong" relationship.

In addition to the correlation coefficients, we conducted a principal component analysis (PCA), a multivariate technique that reduces the dimensionality of large datasets via linear transformation, which allows for feature extraction and data visualization (Jolliffe 2005). Herein, PCA is used to describe which physical and mechanical parameters have similar contributions to variance in the dataset..

Porosity, density, and permeability

Oven-dried specimens were used for measuring dry mass, dry density, unit weight, porosity, and permeability. Porosity was measured using a Micromeritics AccuPyc™ II 1340 helium pycnometer, which measures the specimen's solid volume (V_s). This is subtracted from the total volume (V_t) to determine pore volume (V_p) and connected porosity (φ), as follows: $V_t - V_s = V_p$, and $\varphi = V_p / V_t$. Specimen density was calculated by dividing the mass of each specimen by its total volume (V_t).

For relatively high permeability specimens ($> 10^{17}$ m^2), permeability was measured at room temperature using a steady-state Vinci Technologies benchtop permeameter interfaced with a Bronkhorst El-Flow® volumetric flowmeter. The steady state permeameter records the volumetric flow rate through the specimen core, driven by the pressure differential of nitrogen as the pore fluid upstream, and ambient atmospheric pressure downstream. Specimens were placed in a rubber sleeve in a Hoek cell and radially confined at 1 MPa prior to applying nitrogen gas at a steady pressure to one end of the sample. The radial confinement assured that the nitrogen gas flowed through the specimen and not between the sample edge and the membrane. See Hill (2020) for steady state permeameter setup details. Flow rate measurements were collected at several pressure gradients, allowing permeability to be calculated using Darcy's Law:

$$-\frac{dp}{L} = \frac{(\mu Q)}{A k_D} \tag{3}$$

where *p* is the pressure, *L* is the length of the specimen, A is the cross-sectional area, k_d is the gas permeability, μ is the dynamic viscosity coefficient of the pore fluid, and *Q* is the flow rate.

For lower permeability specimens ($< 10^{-17}$ m^2), permeability was measured using a Core Laboratories PDP-200 pulse decay permeameter at 30 °C. Specimens were placed in a core holder and a uniform confining pressure of ~2 MPa was manually applied with a hydraulic pump to assure that the test fluid moved through the specimen and not between the specimen and the core holder. The system uses nitrogen gas to saturate the test specimen and then the downstream

gas valve is opened, allowing for a pressure differential to develop across the specimen. The system then measures the pressure differential decay across a specimen at regularly timed intervals. Permeability was calculated through a function provided in Brace et al. (1968) as follows:

$$k_{gas} = \left(\frac{2\eta L}{A}\right)\left(\frac{V_{up}}{p_{up}^2 - p_{down}^2}\right)\left(\frac{\Delta p_{up}}{\Delta t}\right) \tag{4}$$

where k_{gas} is gas permeability, η is the viscosity of the pore fluid (nitrogen), Δt is change in time, L is the length of the specimen, A is the cross-sectional area of the specimen, V_{up} is the volume of gas in the upstream reservoir and piping, p_{up} is the pressure of the gas in the upstream reservoir and piping, p_{down} is the pressure of gas in the downstream reservoir and piping, and Δp_{up} is the change in p_{up} during the elapsed time. See Cant et al. (2018) for pulse-decay permeameter setup details.

Magnetic susceptibility

Magnetic susceptibility was measured using a Terraplus KT-10 v2 magnetic susceptibility meter on the natural face and a cut face of each block. The KT-10 m was held in direct contact with either the natural or cut surface of the block in accordance with the manufacturer (see Terraplus User's Guide, v. 2.1), measured three times, and averaged to produce one value per block. Measurements were not made on individual specimens due to the 65-mm coil diameter in the KT-10 m.

Elastic wave velocities and dynamic elastic moduli

Dry compressional (Vp) and shear wave velocities (Vs) were collected using a GCTS CATS interfaced with transducer-mounted piezoelectric quartz crystals operating at a 900 kHz resonance frequency and a 20 MHz pulse sampling rate, with a minimum of 100 waveforms per compression wave type per specimen. Ultrasonic gel and a constant 312 Pa stress were applied to ensure sufficient contact between the specimens and platens to produce consistent waveforms. Dynamic Young's modulus and dynamic Poisson's ratio were calculated as follows (Guéguen and Palciauskas 1994)

$$v_d = \frac{V_P^2 - V_S^2}{2(V_p^2 - V_s^2)} \tag{5}$$

$$E_d = \frac{\rho V_s^2 \left(3V_p^2 - 4V_s^2\right)}{\left(V_p^2 - V_s^2\right)} \tag{6}$$

where v_d is the Poisson's Ratio, V_p is compressional wave velocity, V_s is shear wave velocity, E_d is the Young's Modulus, and ρ is dry bulk density.

Uniaxial compressive strength and static Young's modulus

Dry uniaxial compressive strength (UCS) measurements were conducted on a Technotest 3000 kN servo-controlled loading frame at room temperature. Specimens were tested at a constant strain rate of 1.0×10^{-5} s^{-1}, like other studies of volcanic material (Siratovich et al. 2014; Heap et al. 2015b; Schaefer et al. 2015; Mordensky et al. 2018). Axial strain was measured using a linear-variable displacement transducer extensometer, and static Young's modulus was determined using the average modulus of the linear portion of the stress–strain curve following ASTM standards (ASTM D7012-07).

Triaxial compressive strength, friction angle, cohesion, and intact rock constant m$_i$

Three specimens from each block were tested in conventional triaxial conditions ($\sigma_1' > \sigma_2' = \sigma_3'$, in which σ_1' is the major effective principal stress, σ_2' is the intermediate effective stress, and σ_3' is the minor effective principal stress) over a limited range of confining stresses (σ_3'), with no confining stress larger than 50% of the average UCS of the block (as determined using by calculating the average UCS of specimens tested from the same block) to ensure that failure remains in the brittle regime (Labuz and Zang 2012; Hoek and Brown, 1980; Hoek and Brown 1997). Dry triaxial compressive strength measurements were conducted using a Hoek cell and deformed with a Technotest 3000 kN servo-controlled loading frame at a constant strain rate of 1.0×10^{-5} s^{-1} at room temperature. Common confining stresses of 2, 3, 5, 10, 20, 22, or 25 MPa were used, when possible, to allow for comparison between samples. Results from the triaxial laboratory experiments were analyzed with the Rocscience RSData software to calculate material constant m$_i$, friction angle and cohesion for each block. The material constant m$_i$ was calculated using the Hoek–Brown failure criterion for intact rock with the modified cuckoo curve fitting method and basic error summation method (see Supplementary Table 2 for RocData processing results). Friction angle and cohesion were calculated using the linear curve fitting method and vertical error summation method (see Supplementary Table 3 for RocData processing results).

Results

Blocks were categorized by volcanic lithology, which distinguishes rocks by physical characteristics resulting from depositional or emplacement processes. Herein, we use the

following terms: 'lavas' are former molten rocks expelled at the Earth's surface by volcanic processes; 'autoclastic breccias' are rocks formed during effusive volcanism when a lava flow cools and fragments in contact with air, and the fragments are deposited under continued lava flowage; 'pyroclastic rocks' are rocks containing fragments formed from volcanic plumes, jets, or pyroclastic density currents as particles first come to rest via suspension settling, traction, and/or en masse freezing (Fisher 1961; White and Houghton 2006). In total, we present the physical and mechanical characteristics of 17 lavas (one being ejected block RH50 as described in the Materials and Methods section), 5 autoclastic breccias, and one pyroclastic rock, which is a scoria. While the pyroclastic sample is included in the following presentation of the laboratory results, we caution the reader on over-interpreting patterns related to pyroclastic rock, since there is only one sample in this lithologic category.

Alteration mineralogy and classification

The laboratory-based spectroscopy results show that the blocks contain distinct absorption features around 1410–1450 nm, 1920 nm, and within the broader spectrum between 2180–2400 nm (Fig. 3a), indicating the presence of phyllosilicates (clays) including kaolinite, halloysite, smectites (mostly montmorillonite and nontronite), and minor illite (see Douglas et al. 2022, and references therein). The samples also occasionally contain minor absorption features around 2180 and 2265 nm, which are due to the presence of alunite and jarosite, respectively (Fig. 3a). More commonly, the samples have absorption features in the visible region, notably around 390, 425, 485, and 540 nm, which are consistent with minerals such as sulfur, goethite, and hematite (Fig. 3a). Based

on SEM–EDS analysis, some samples have disseminated pyrite, occurring together with silica polymorphs (e.g., RH28, RH38, Fig. 3d, e). These minerals do not have any strong characteristic absorption features in the visible and shortwave-infrared regions. Alteration minerals are often limited to vugg and fracture infills and occur as replacement products of the rock's matrix, and partial to full replacement of the original mineralogy (Fig. 3d, e). A detailed characterization of sample alteration mineralogy, including a conceptual model of alteration history at Ruapehu, is described in detail in Kereszturi et al. (2020).

Following the weathering/alteration assemblages, defined by indicator minerals (minerals specific to certain weathering, oxidation, and hydrothermal alteration processes), their occurrence, and their origin (Rye 2005; Simmons et al. 2005) samples were categorized into four mineral assemblages (Table 2): (1) Fresh, consisting of primary mineralogy such as pyroxene, plagioclase, and titanomagnetite; (2) Surface weathering, consisting of primary and chemically weathered and oxidized minerals including Fe-oxides (hematite) and minor smectites typically occurring in a weathered rim; (3) Supergene, argillic alteration that develops at < 40 °C through long-term weathering and oxidation of ferrous and minor sulfide-bearing rocks in atmospheric conditions, which includes phyllosilicates, jarosite, and Fe-oxides; (4) Steam-heated, intermediate and advanced argillic alteration that develops at < 120 °C near the water table and in the shallowest epithermal environment, including, quartz, pyrite, Fe oxides (goethite), phyllosilicates, sulfur, and occasional jarosite and alunite (Table 2). The latter two categories often show mineral overprinting, when rocks subjected to hypogene conditions are later subjected to weathering and erosion, resulting in the replacement of some meta-stable hydrothermal minerals (e.g., pyrite to jarosite;

Table 2 Weathering/alteration category and associated mineral assemblages of collected sample blocks

Category	Mineralogy	Occurrence and origin	Blocks
Fresh	Primary (pyroxene, plagioclase, titanomagnetite)	Volcanic processes, minor surface weathering and/or oxidation	RH17, RH17b, RH19, RH42b
Surface weathering (weathered rim)	Primary and chemically weathered including smectites	Weathering of primary volcanic rocks with various percentages of primary (typically interior of sample) to weathered or oxidized (typically exterior/crust of sample) material	RH2, RH2b, RH4, RH5, RH6, RH8, RH9, RH10, RH15, RH16
Supergene (argillic)	Phyllosilicates, jarosite, Fe oxides	Develops at < 40 °C through weathering and oxidation of sulfide-bearing rocks in atmospheric conditions	RH14, RH11, RH21, RH22, RH52b
Steam-heated (intermediate to advanced argillic)	Alunite, jarosite, opal, pyrite, Fe oxides, phyllosilicates, sulfur	Develops at < 120 °C near the water table and in the shallowest epithermal environment through alteration by steam-heated acid-sulfate waters	RH28, RH38, RH50, RH52

schwertmannite and goethite/hematite; anhydrite to gypsum) in atmospheric pressure and temperature conditions.

In addition to various mineral assemblages, samples also showed variations in alteration pervasiveness. Thus, samples were also categorized into four groups based on the extent of weathering/alteration, including "none" (fresh material), "minor" (typically only the exterior/crust of the sample is weathered or altered), "moderate" (weathering or alteration is present throughout the groundmass), and "pervasive" (weathering or alteration is strongly present in groundmass and crystals) (Table 3). Surface weathering samples have varying percentages of total weathered material, with autoclastic breccias (e.g., samples RH4, RH6) and the tephra (RH15) being more pervasively weathered than lavas (e.g., samples RH2b, RH2, RH5, RH8, RH10, RH16) due to pre-existing fractures, smaller grain size, and more void space.

Physical and mechanical characterization

Block averaged properties are shown in Table 3, and properties for each specimen (individual cores) are available in Supplementary Table 1. Individual parameters are plotted against either porosity (Figs. 4 and 5) or Vp (Fig. 6), which systematically have the highest correlation factors to other physical and mechanical properties (Fig. 7).

Porosity, permeability, density, and magnetic susceptibility results are as follows:

- The average connected porosity of all specimens ranges from 1.6-48.3%, highlighting the heterogeneity of the sample suite (Figure 2, Figure 4, Table 3).
- Porosity is generally higher in autoclastic breccias and pyroclastic rocks (c. 22-48 %) than lavas (c. 2-30 %) (Figure 4a).
- Porosity is highest in rocks with surface weathering (average = 18%) (Figure 4b) and pervasive alteration (average = 28%) (Figure 4c).
- The standard deviation of porosity between specimens is below 2%, except for RH6 (SD = 3%) and RH19 (SD = 3.2%).
- Specimen dry mass density generally increases with decreasing values of porosity, ranging from 1.37 to 2.67 g/cm^3.
- Permeability exhibits 6 orders of magnitude difference between the lowest (4×10^{-18} m^2) and highest (3×10^{-12} m^2) permeable specimens (Figure 5a-c).
- Lavas typically have lower permeability ($< 1 \times 10^{-14}$ m^2) than autoclastic breccias and pyroclastic rocks ($> 1 \times 10^{-14}$ m^2) (Figure 5a). Despite this trend, the permeability of rocks with similar porosities can vary by up to two orders of magnitude.
- Magnetic susceptibility ranges from 0 to 0.04 SI, with a weak relationship with porosity (Figure 5d-f).

- Pervasively altered and steam-heated blocks have lower magnetic susceptibility than less altered or unaltered blocks, and lavas have higher magnetic susceptibility than autoclastic breccias and pyroclastic rocks (Figure 5d-f).

Dry Vp and Vs are inversely related to porosity, with Vp and Vs velocities typically being higher in lavas than autoclastic breccias and in the pyroclastic rock (Fig. 5m-o, Fig. 6, Table 3); all lava Vp are > 3600 m/s and Vs are > 1300 m/s, while autoclastic breccias have Vp < 3400 m/s and Vs < 1400 m/s, apart from RH42b with a Vs of 1661 m/s. The relationship of Vp and Vs with porosity has been previously established (e.g., Heap et al. 2014a, b; Wyering et al. 2014; Mordensky et al. 2018). Additionally, Vp and Vs are lowest in pervasively altered samples, but do not systematically vary with alteration pervasiveness or alteration type (Fig. 6b-c), as has been shown by previous studies (Wyering et al. 2014). Similar patterns exist for dynamic Poisson's ratio and dynamic Young's modulus, which range between 0.23–0.46 and 7.1–32.1 GPa, respectively. Static Young's modulus shows a wider range than dynamic Young's modulus, varying between 3.7–42.3 GPa. Again, static Young's modulus is significantly higher in lavas (average = 23 GPa) than in autoclastic breccias and the pyroclastic rock (average = 7.5 GPa), is closely dependent on porosity (Fig. 5g-i), shows weak systematic decreasing trends with increasing alteration type and pervasiveness, and has a strong relationship to Vp (Fig. 6d-f). Dynamic Young's modulus values tend to be higher than static Young's modulus, although this is reversed for stiffer material (values > 25 GPa) (Fig. 8).

Uniaxial compressive strength (UCS) correlates with porosity (Fig. 7), with UCS decreasing exponentially with increasing porosity (Fig. 4). In lower-porosity samples (< 10%), UCS can vary by over 200 MPa. Variations in UCS for samples with > 10% porosity are much smaller (~ 50 MPa max). UCS at low porosity (< 20%) decreases with an increase in the pervasiveness of weathering or hydrothermal alteration, and fresh material is stronger than surface weathering and supergene alteration, all of which are stronger than steam-heated material. Again, there can be large ranges of UCS values within these alteration categories, and the trends described do not apply to material > = 20% porosity.

Triaxial experiment results are shown in Fig. 9 and summarized in Table 4. These experiments show that sample strength increases with increasing confining pressure (Table 4, Fig. 9e-f). Stress–strain curves show that fresh and altered lava samples exhibit brittle mechanical behavior (Fig. 9a) at low confinement, where a peak stress (differential stress) is reached followed by strain softening (as described in Wong and Baud 2012). While fresh breccias also display brittle mechanical behavior at low confinement, altered breccias display ductile behavior (Fig. 9b),

Table 3 Descriptions and average physical and mechanical laboratory results for each sample block

| No	Block	Volcanic lithology	Mineral phases	Weathering/alteration category (see Table 2)	Extent of weathering/alteration	Magnetic susceptibility	Density (kg/m^3)	Porosity (%)	Permeability (m^2)	Vp (m/s)	Vs (m/s)	UCS (MPa)	Static Young's modulus (GPa)	m$_i$	Friction angle (°)	Cohesion (MPa)
1	RH2	lava	minor phyllosilicate and Fe oxidation	surface weathering	minor	0.0155	2361	14.7	2.23E-16	4160	2029	98.38	22.07	16.08	47.87	18.89
2	RH2b	lava	minor phyllosilicate and Fe oxidation	surface weathering	minor	0.0221	2652	5.59	4.03E-18	4450	1452	258.14	32.13	32.97	54.36	39.89
3	RH4	autoclastic breccia	goethite, minor phyllosilicate	surface weathering	pervasive	0.0072	2077	24.62	6.51E-13	2346	1325	26.81	8.4	24.27	51.72	4.6
4	RH5	lava	goethite, minor phyllosilicate	surface weathering	minor	0.017	2595	6.07	3.06E-17	5246	1450	161.08	30.56	38.57	55.64	28.61
5	RH6	autoclastic breccia	minor phyllosilicate	surface weathering	pervasive	0.0018	1722	39.95	6.19E-13	2329	1377	10.54	3.86	12.47	45.3	2
6	RH8	lava	geothite, minor phyllosilicate	surface weathering	minor	0.0202	2228	19.45	6.65E-17	3731	1962	61.26	18.3	21.19	50.49	10.54
7	RH9	lava	geothite, minor phyllosilicate	surface weathering	minor	0.0258	2517	9.14	6.65E-17	5193	2424	111.65	24.03	25.17	52.05	19.61
8	RH10	lava	jarosite, geothite and minor phyllosilicate (kaolinite)	surface weathering	minor	0.0196	2569	6.59	6.26E-18	5241	2074	200.42	29.2	33.52	54.49	34.6

Table 3 (continued)

No	Block	Volcanic lithology	Mineral phases	Weathering/alteration category (see Table 2)	Extent of weathering/alteration	Magnetic susceptibility	Density (kg/m³)	Porosity (%)	Permeability (m²)	Vp (m/s)	Vs (m/s)	UCS (MPa)	Static Young's modulus (GPa)	m_i	Friction angle (°)	Cohesion (MPa)
9	RH11	lava	geothite, Al and Fe rich phyllosilicate (kaolinite), and minor jarosite	supergene	moderate	0.0062	2505	9.44	3.62E-17	4706	1836	110.72	17.04	28.87	53.24	18.93
10	RH14	lava	minor phyllosilicate, ferrihydrite and Fe oxidation	supergene	moderate	0.0109	2425	9.44	4.33E-15	3963	1883	150.23	26.09	14	46.49	27.36
11	RH15	pyroclastic (scoria)	fresh rock with minor phyllosilicate and Fe oxidation	surface weathering	minor	0.01	1372	48.25	2.98E-12	2715	1373	7.79	4.39	21.05	50.43	1.75
12	RH16	lava	fresh rock with minor phyllosilicate and Fe oxidation	surface weathering	minor	0.0118	2440	8.73	1.10E-16	3955	1987	118.87	25.93	27.29	52.75	20.12
13	RH17	lava	fresh rock with minor Fe oxides	fresh	none	0.0114	2521	6.32	8.02E-17	4271	1829	182.19	27.35	47.58	57.27	30.98
14	RH17b	lava	fresh rock with minor Fe oxides	fresh	none	0.0097	2623	1.57	8.02E-17	4563	1768	312.42	42.3	32.32	54.19	52.43

Table 3 (continued)

No	Block	Volcanic lithology	Mineral phases	Weathering/alteration category (see Table 2)	Extent of weathering/alteration	Magnetic susceptibility	Density (kg/m³)	Porosity (%)	Permeability (m²)	Vp (m/s)	Vs (m/s)	UCS (MPa)	Static Young's modulus (GPa)	m_i	Friction angle (°)	Cohesion (MPa)
15	RH19	autoclastic breccia	fresh rock with minor phyllosilicate and Fe oxidation	fresh	none	0.0125	2166	22.46	4.20E-14	3342	1287	40.48	9.1	32.36	54.2	7.58
16	RH21	lava	goethite, Fe-rich phyllosilicate and minor jarosite	supergene	minor	0.0431	2668	6.77	2.06E-17	4503	1904	147.8	18.66	31.41	53.95	25.45
17	RH22	lava	jarosite, ferrihydrite, and minor Fe-rich phyllosilicate	supergene	moderate	0.007	1985	30.43	2.33E-12	3607	1380	33.8	7.21	7.44	39.61	7.45
18	RH28	autoclastic breccia	montmorillonite, geothite, pyrite, quartz, and minor kaolinite	steam-heated	pervasive	0.0027	1661	42.72	4.93E-14	2614	1394	12.69	3.72	16.84	48.32	2.05
19	RH38	lava	geothite, pyllo-silicate, pyrite, quartz, and minor jarosite	steam-heated	moderate	0.0102	2416	19.61	1.18E-16	4249	1791	81.03	13.89	22.49	51.04	14.06

Table 3 (continued)

No	Block	Volcanic lithology	Mineral phases	Weathering/alteration category (see Table 2)	Extent of weathering/alteration	Magnetic susceptibility	Density (kg/m³)	Porosity (%)	Permeability (m²)	Vp (m/s)	Vs (m/s)	UCS (MPa)	Static Young's modulus (GPa)	m_i	Friction angle (°)	Cohesion (MPa)
20	RH42b	autoclastic breccia	geothite, jarosite	fresh	none	0.0061	1826	33.35	4.11E-16	3374	1661	47.71	15.43	5.93	36.93	11.12
21	RH50	lava (block)	alunite, jarosite, sulfur, and minor geothite, phyllosilicate (e.g. kaolinite, hallosite)	steam heated	pervasive	0.0009	2292	3.64	2.19E-17	4395	2001	91.98	17.77	13.29	45.96	17.07
22	RH52	lava	goethite, minor sulfur, barite, phyllosilicate, pyrite, quartz and minor jarosite	steam-heated	moderate (primarily outer 6 mm)	0.0103	2650	2.84	1.35E-16	4765	1797	132.47	21.74	25.25	52.07	23.04
23	RH52b	lava	ferrihydrite, minor phyllosilicate	supergene	moderate	0.0073	2285	17.38	2.10E-16	3638	1491	66.24	15.07	13.6	46.2	12.21

Fig. 4 Porosity vs. uniaxial compressive strength (UCS) of all tested specimens, split into (**a**) lithology, (**b**) weathering/alteration mineralogy, and (**c**) weathering/alteration mineralogy. Porosity-UCS trend outliers RH50 and RH52 are discussed in the text
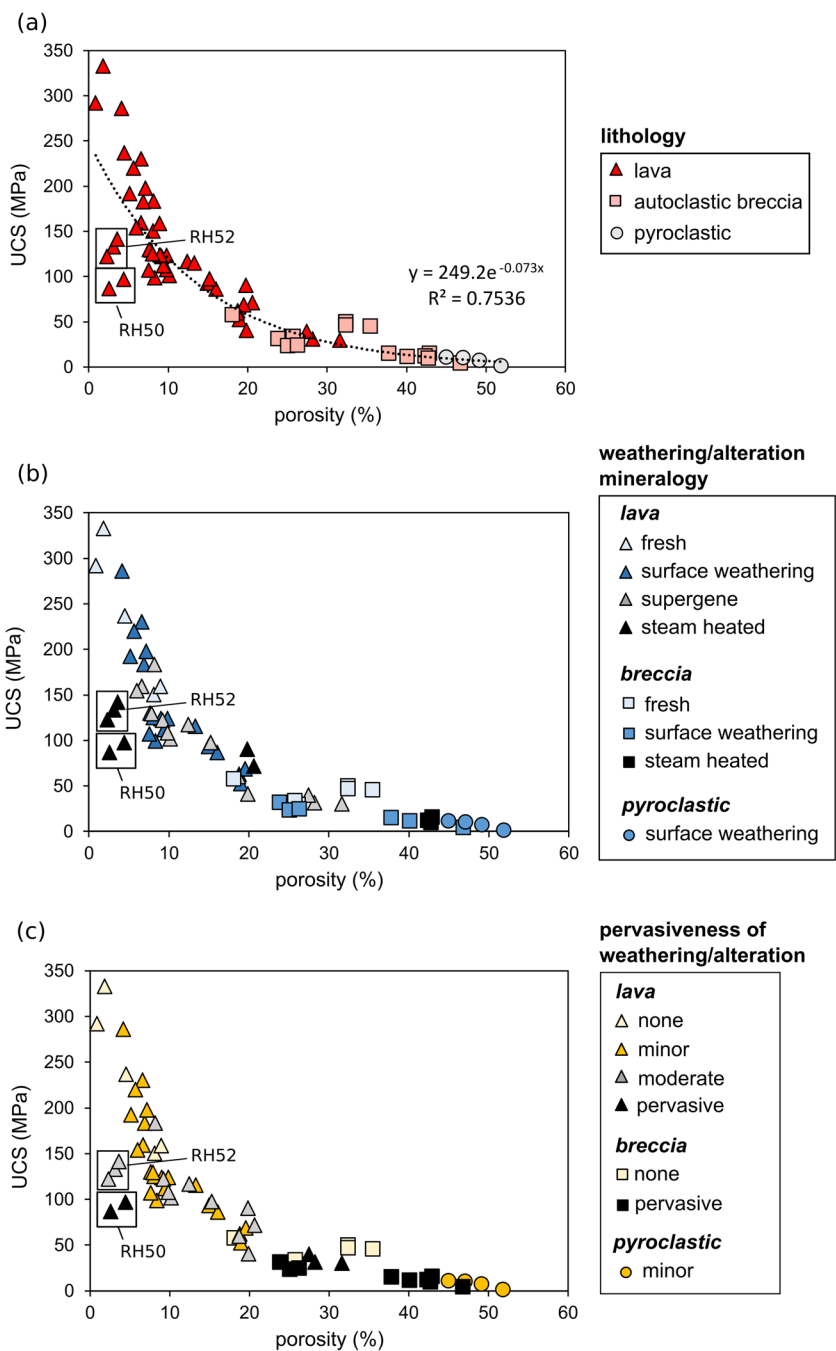
characterized by an absence of strain softening and dilation, and where failure is a function of compactant pore collapse (as described in Heap et al. 2015a). Unaltered lavas tend to be strong, stiff and with low porosities, while altered lavas tend to be weak, ductile or have high porosities (Fig. 9a-b, e–f), and samples with similar porosities tend to have similar strength values at a given confining pressure (Fig. 9c-d). Altered samples tend to reach lower peak stress, have a less defined failure peak, or experience higher strains than fresh samples (Fig. 9a-b, e–f), although deviations from these patterns do occur.

Cohesion covers a wide range of values from 1.8 to 52.4 MPa (Table 3), which has a positive correlation with UCS (Fig. 7) and a positive logarithmic relationship with V_p (Fig. 6g-i). Like UCS, cohesion is higher in lavas than autoclastic breccias and in the pyroclastic rock and decreases with increasing weathering and alteration pervasiveness. Friction angle ranges from 37 to 57° (Table 3) and has a positive and monotonic (in this case logarithmic) relationship with intact rock parameter m_i (Fig. 7). Intact rock parameter m_i ranges from 6 to 48 (Table 3) and has a weakly negative monotonic correlation with porosity (Fig. 7), but no clear
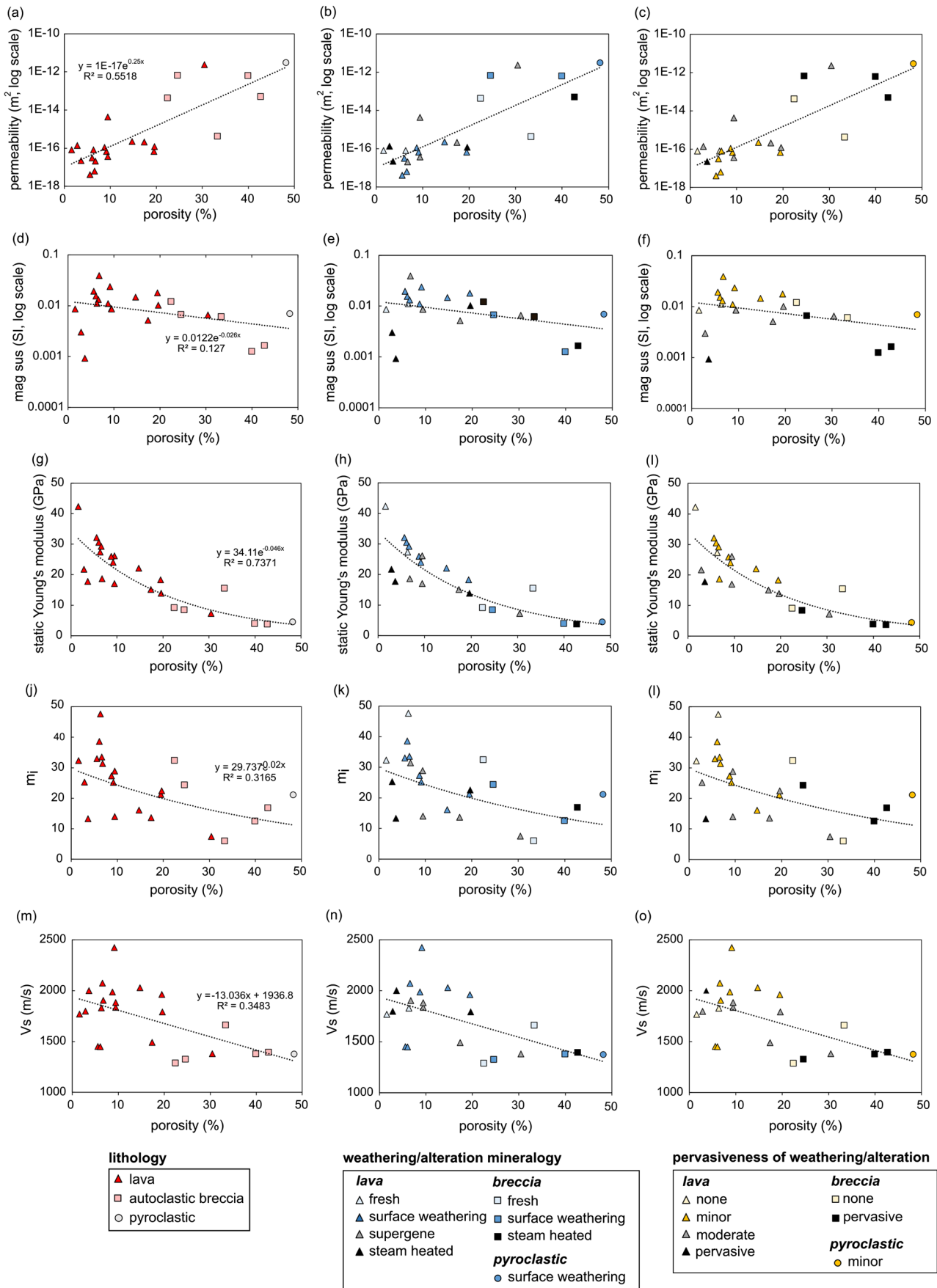
◄**Fig. 5** Relations of various averaged block properties vs. averaged block porosity, split into columns according to lithology, weathering/alteration type, and weathering/alteration pervasiveness. (**a-c**) Porosity vs. permeability. (**d-f**) Porosity vs. magnetic susceptibility. (**g-i**) Porosity vs. static Young's modulus. (**j-l**) Porosity vs. Generalized Hoek–Brown failure criterion intact rock constant m_i. (**m–o**) Porosity vs. Vs

relation to rock texture, alteration type or pervasiveness when plotted against porosity (Fig. 5j-l).

PCA results (Fig. 10) group the physical and mechanical parameters in terms of similar impacts on the variance of the dataset. The results are presented as a set of biplots for the first three principal components to encompass a significant proportion of the variance, as well as to identify principal components for which parameters correlate and do not correlate. The directions of the arrows represent the eigenvectors of the analysis. Parameters that correlate tend to have arrows pointing in the same or opposite directions. Parameters that do not correlate tend to have arrows pointing in orthogonal directions. The biplots show that, for three combinations of the first three principal components (representing 80% of the variance), parameter groupings remain quite consistent, although some of the trends are stronger for different combinations. The physical and mechanical property relations revealed in these graphs is discussed below.

Discussion

Weathering and alteration mineralogy

The predominant weathered/altered minerals identified by infrared spectroscopy are Fe-bearing oxides and clay mineral associations typical of acid-sulfate alteration processes (e.g., kaolinite, smectites), producing argillic to advanced argillic alteration of the primary volcanic rocks (Heald et al. 1987; Simmons et al. 2005). The alteration minerals form through supergene to hypogene weathering and/or alteration of the host rocks that originally contain plagioclase, minor pyroxene, (titano-)magnetite, and rarely olivine, amphibole phenocrysts and microcrystals in the groundmass (Fig. 3). Phyllosilicates, sulfides, and sulfates are consistent with acidic and steam-heated environments, such as the currently active vent-hosted system underneath Ruapehu's Crater Lake (Christenson and Wood 1993; Christenson 2000), which precipitates such alteration minerals via oxidation of H_2S and H_2SO_4-rich fluids by atmospheric oxygen at shallow depths.

Samples show a strong shift in the position of the Fe^{3+} iron absorption from 530 nm (e.g., hematite-dominated) to shorter wavelengths around 480 nm (e.g., goethite-dominated), as hydrothermal/weathering alteration increases (Fig. 3). This spectral shift is indicative of the pH preference of these indicator minerals (e.g.,

hematite-dominance in less-acidic and neutral pH conditions; Schwertmann and Murad 1983) and the presence of disseminated pyrite formed through acid-sulfate alteration, which may later undergo supergene oxidation, resulting in the formation of Fe-oxides (goethite), jarosite, gypsum, and smectite (Fernandez-Caliani et al. 2004; Rye 2005). Spectral peaks at 2160–2210 nm, 2315 nm, and 2390 nm for samples with increased clay content (e.g., kaolinite, smectites) are associated with longer exposures to weathering or hydrothermal fluids. This is consistent with the present-day geology of Ruapehu, where ancient hydrothermal systems can be partially covered by younger volcaniclastic and lava rocks (Kereszturi et al. 2020).

Physical and mechanical property relations

Physical and mechanical test results reveal several common relations between material properties (Tables 3 and 4, Figs. 4, 5, 6, 7, 8, 9 and 10). As shown in the PCA results (Fig. 10), measured UCS and calculated σ_{ci} always plot together, highlighting that they could be interchanged depending upon which is available. They tend to plot in the vicinity of the other strength parameters, cohesion, and elastic parameter static Young's modulus. Friction angle and m_i also consistently plot close to each other because they represent the shape, and slope and curvature, respectively, of the failure criterion to which each belongs. Porosity and permeability also tend to coincide, whereas density and Vp consistently plot in the opposite direction, highlighting the inverse impact of porosity on density and Vp, and its positive impact on permeability. Dynamic Young's modulus and Vs tend to plot in similar locations, which are often orthogonal to the other parameter directions, suggesting that there is low correlation to other parameters. Magnetic susceptibility does not have any consistent relationships with the other parameters; for some principal component combinations it plots near or parallel to some parameters (e.g., density and porosity in Fig. 10a), and for other combinations it plots away from all other parameters (e.g., Fig. 10c).

Similar to other studies, we find that porosity has a first-order effect on other physical and mechanical properties, including strength and stiffness, permeability, and rock failure mode (Al-Harthi et al. 1999; Pola et al. 2012; Heap et al. 2014a, 2014b, 2015b, 2019a; Schaefer et al. 2015; Siratovich et al. 2016; Cant et al. 2018; Coats et al. 2018; Mordensky et al. 2018). UCS and Young's modulus decrease exponentially with increasing porosity, while permeability increases exponentially with porosity (Fig. 4, Fig. 5a-c, g-i). Low porosity samples also generally have higher values of Poisson's Ratio, m_i, magnetic susceptibility, and Vp. Lavas typically have
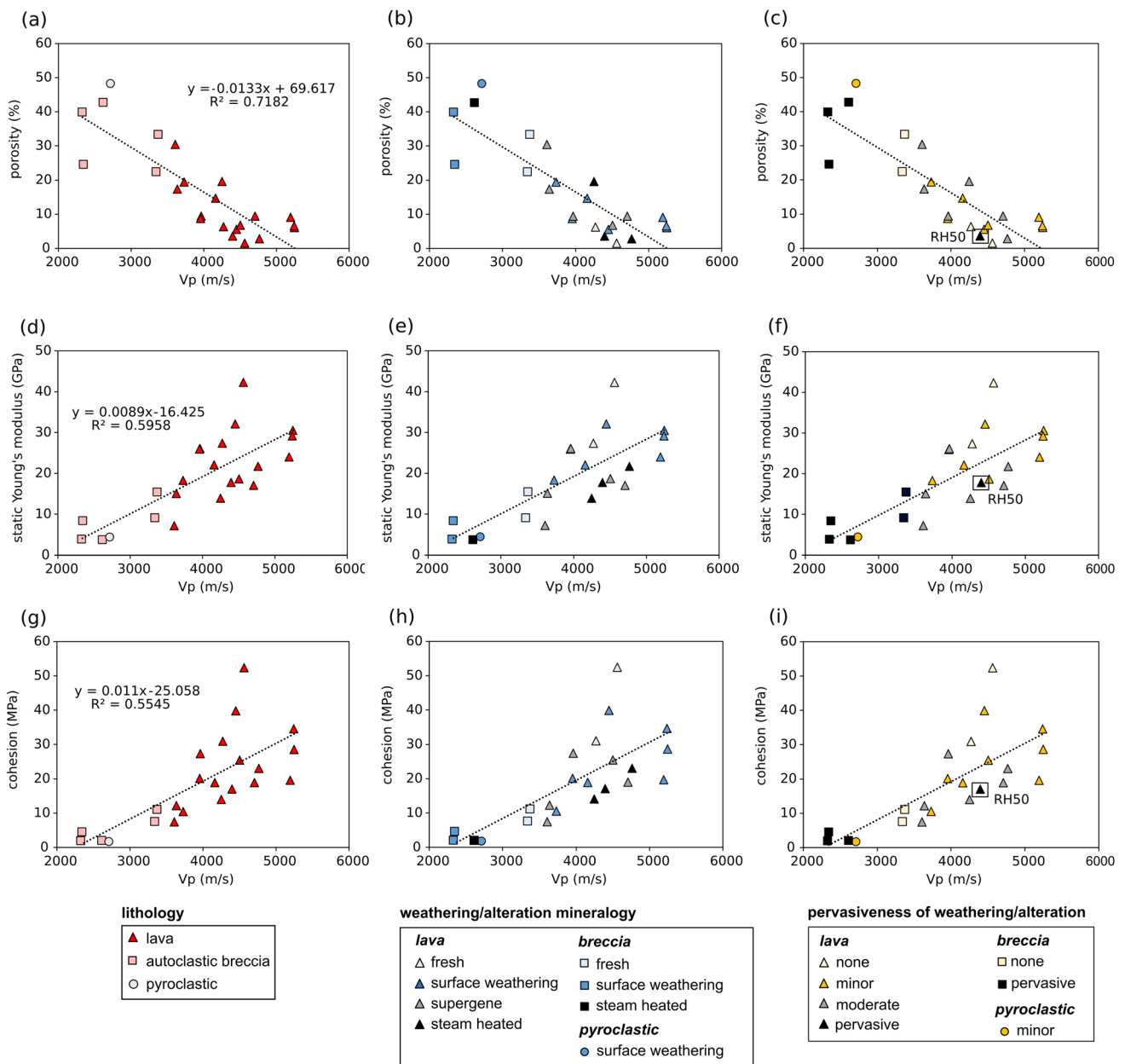
Fig. 6 Relations of various averaged block properties vs. averaged block P-wave velocity (Vp), split into columns according to lithology, weathering/alteration type, and weathering/alteration pervasiveness. (**a-c**) Vp vs. porosity. (**d-f**) Vp vs. static Young's modulus. (**g-i**) Vp vs. cohesion. Outlier RH50 in pervasiveness of weathering/alteration graphs is discussed in the text

lower porosities (< 20%) than autoclastic breccias and the pyroclastic rock (> 20%), mostly due to emplacement mechanisms; the slow cooling of lava flows allows gas bubbles to escape and coalesce prior to solidification, resulting in lower porosity, while pyroclastic rocks freeze and fragment rapidly with the bubbles still distributed throughout the clast, resulting in higher porosity. Thus, lithology (i.e., lava versus autoclastic breccia) additionally correlates to material properties (Figs. 4, 5 and 6; as in Mordensky et al. 2018). However, it should be stressed

that, within each of these categories, properties can vary significantly, as also highlighted by the variability in the direction of the density eigenvectors compared to the other parameters in Fig. 10. For example, in low porosity samples (lavas with porosity < 10%), UCS can vary by over 200 MPa. Even within 6–7% porosity, sample peak stress can vary by 100 MPa (Fig. 9c). Clearly, other parameters have more impact on strength at low porosity.

Vp, density, and Young's modulus also show strong relationships with many material properties (Fig. 5g-i, Fig. 6,

Fig. 7 Correlation matrices between average block parameters, showing (**a**) linear (Pearson) and (**b**) monotonic (Spearman rank) relationships between variables. Legend indicates strength of correlation coefficient (ranging from black/value of 1: high correlation to white/value of 0: weak correlation). Sample RH50, which originated from the upper conduit and thus is considered a subsurface sample, is not included in these matrices

(a)

(b)
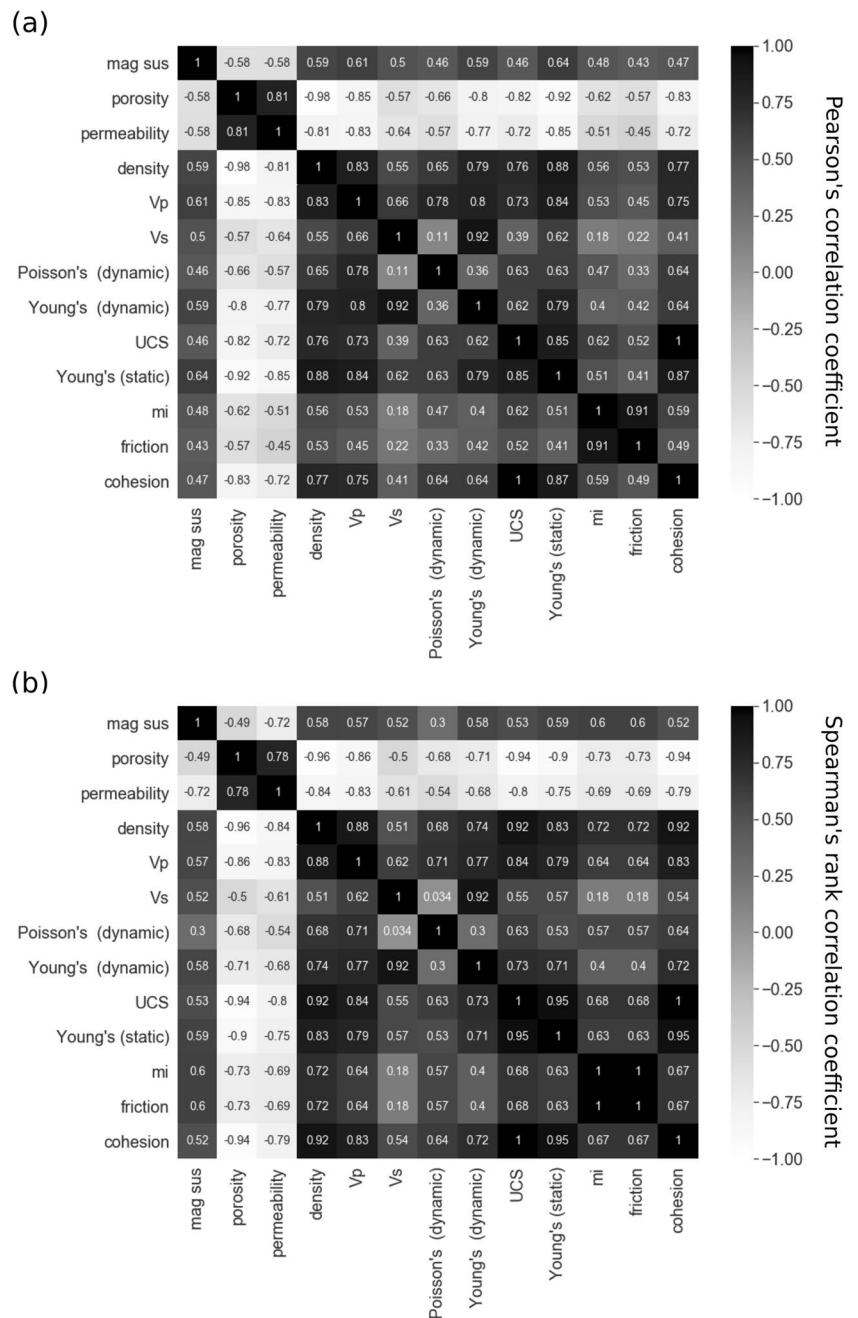
Fig. 7). Seismic velocities in volcanic rocks typically attenuate with the presence of glass, clay alteration, microcracks, and vesicles (Vanorio et al. 2002; Pola et al. 2012). Like other authors (Wyering et al. 2014), we find that the correlations between Vp and porosity, density, and permeability are strong. Correlations of Vs with other properties is weaker than Vp, likely because of errors related to the difficulty in picking the first arrival of the S-wave, leading to a large dispersion of Vs values (Vilhelm et al. 2016), which also affects the dynamic Young's modulus and dynamic Poisson's ratio, reducing potential for deriving transfer functions from these parameters. Static Young's modulus correlates

well with Vp, density, and strength (Fig. 7). Density, and dynamic Poisson's ratio and Young's modulus calculated from seismic velocities, show similar but weaker relations compared to static Young's modulus (Fig. 7), likely arising from the dispersion of Vs. We find that magnetic susceptibility has a moderate to weak relationship with Young's modulus (Fig. 7), and porosity and density (Fig. 5d-f, Fig. 7), although the relationship with Young's modulus may be the result of porosity rather than a truly independent relationship. The correlation of magnetic susceptibility with porosity and density for a given rock type is well established (Henkel 1994); in our samples, it likely stems from

Fig. 8 Static vs. dynamic Young's modulus values. Dynamic Young's modulus values tend to be higher than static Young's modulus, although more stiff material (values > 25 GPa) tends to have higher static Young's modulus values
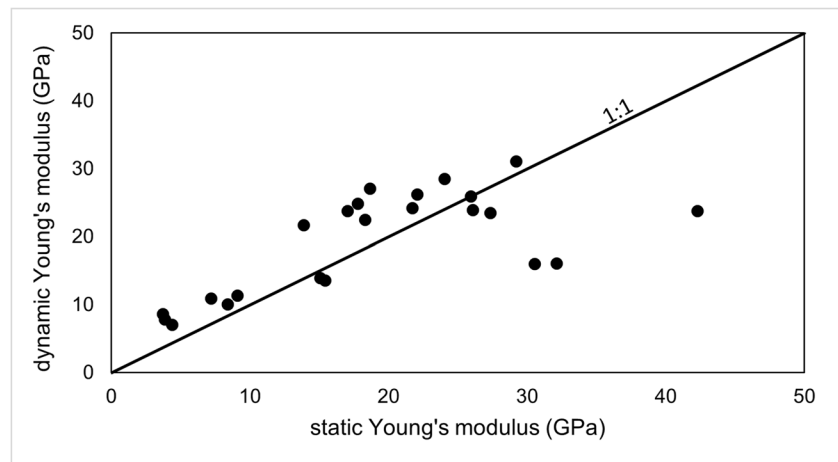
magnetic mineral oxidation and alteration, as well as with lower porosity but also lower density, non-magnetic clay minerals replacing primary magnetic minerals (e.g., titanomagnetite). The relationship of magnetic susceptibility with other material properties is generally weak (Fig. 7, Fig. 10), although lavas tend to have higher magnetic susceptibility values than autoclastic breccias and the pyroclastic rock.

Friction angle and m_i correlate well to each other, as expected, but not to any other parameters (Fig. 7), except weakly with porosity (Fig. 5j-l; Villeneuve and Heap 2021). Interestingly, friction angle and m_i do not appear to correlate for combinations of PC1&PC2 nor PC1&PC3 but do correlate for the PC2&PC3 combination (Fig. 10), suggesting that generating a transfer function for friction angle and m_i is possible but not trivial. Cohesion correlates to UCS as expected, since they both describe the low-confinement strength components of the failure criterion to which each belongs, as well as Young's modulus, density (Fig. 5g-i), Vp (Fig. 6d-f), and porosity (Fig. 7), as also shown in Villeneuve and Heap (2021). The PCA analysis shows, however, that the correlations between strength (UCS) and physical parameters are not consistent across the three principal components examined, suggesting complex relationships. This is the first research that attempts to link m_i to alteration and weathering of volcanic rocks. Although m_i has been thoroughly studied for other crystalline and sedimentary rocks (e.g., Cai 2010; Richards and Read 2011; Carter 2020), most of these studies focus on deriving m_i from lab data or novel methods for estimating it using rock texture (e.g., porosity). Richards and Read (2011) provide a clear discussion regarding the wide variability of this parameter, and this research highlights that, although all of the tested samples are andesite, they vary considerably in terms of their texture and mineralogy, leading to a wide range of m_i. Villeneuve et al. (2021) and Villeneuve and Heap (2021) show that, for these rock types, where triaxial data are

not available, porosity is a potential indicator of m_i (as also shown in Fig. 5j-l), but the wide variation of m_i for a given porosity highlights that m_i depends on several factors, in addition to porosity. As with strength, m_i tends to be higher for fresh rocks than for weathered and altered rocks, which is most pronounced for low-porosity lava (Fig. 11). This shows that more research is required to decipher the links between failure criterion parameters and physical characteristics to improve on empirical data and provide reliable means to estimate these parameters in the absence of triaxial testing, as is often the case in volcano studies.

The influence of weathering and alteration on physical and mechanical properties

While the extent of altered or weathered minerals is in large part due to fossil hydrothermal systems, we find that lavas are less pervasively weathered/altered than autoclastic breccias and the pyroclastic rock (Fig. 4c). In addition to having more void space, autoclastic breccias and the pyroclastic rock also have more incipient micro-fractures (Mordensky et al. 2018), both of which increase permeability (Fig. 5a) and surface area (Farquharson et al. 2019), creating larger reactive surface areas and enabling the circulation of fluids. Scoria (or pumice in dacitic to rhyolitic environments) fragments large enough to core and study mechanically are rare (del Potro and Hürlimann 2008). Additionally, many pyroclastic rocks are too soft or incoherent to be cored. Thus, this study was limited in pyroclastic sampling, which limits our ability to derive patterns in their physical and mechanical properties.

Fresh rock tends to be less porous and stronger than rock with surface weathering, which is less porous and weaker than rock with supergene or steam-heated advanced argillic weathering (Fig. 4b, Fig. 9a-b, Fig. 11a-b, g-h). A larger percentage of weathering and
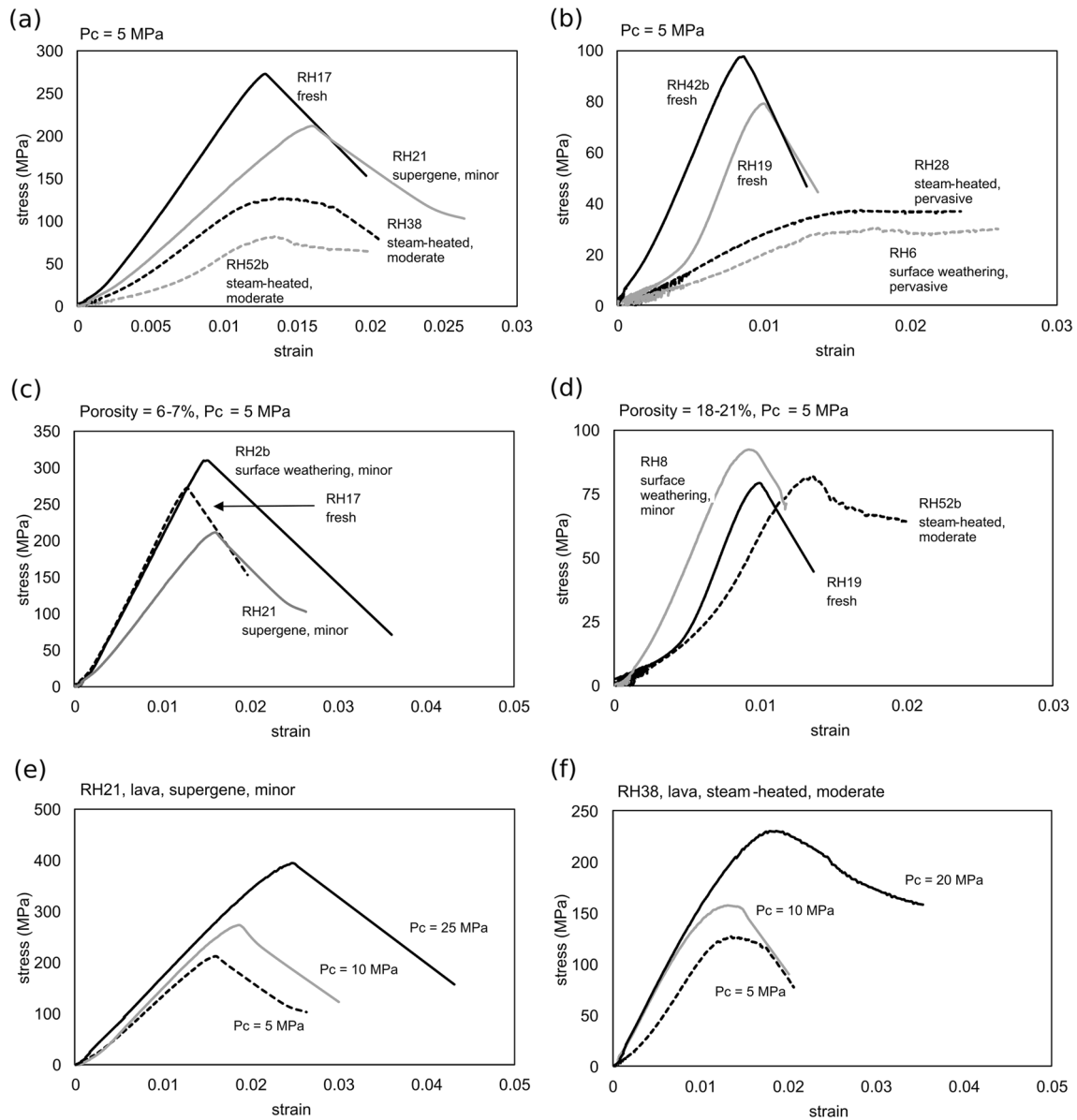
Fig. 9 Stress–strain mechanical data from triaxial experiments. (**a**) Variably altered lava samples at a confining pressure (Pc) of 5 MPa (**b**) Variably altered autoclastic breccia samples also at Pc = 5 MPa.

(**c**) Low porosity samples at Pc = 5 MPa (**d**) high porosity samples at Pc = 5 MPa. (**e**) Minor supergene and (**f**) moderate steam-heated lava sample behavior at three confining pressures

alteration to clay minerals generally reduces strength and increases the propensity for ductile behavior (Fig. 4c, Fig. 9a-b, e–f, Fig. 11g-h; as also observed by Siratovich et al. 2016; Mordensky et al. 2019a), with the degree/intensity of clay alteration negatively correlating to UCS and Young's modulus (Fig. 11g-j; as also observed by Watters et al. 2000). Alteration mineralogy is not solely a function of the primary lithology, being also dependent on the local hydrothermal history of the volcano. Thus, there are limitations to assuming that all steam-heated rocks will be weaker than all fresh rocks, as primary porosity and rock history needs to be taken into

consideration. In our dataset, this is clear in the strong scatter within the minor and moderate alteration pervasiveness categories, and in surface weathering and supergene weathering categories (Fig. 11g-h).

Some characteristics, such as UCS, static Young's modulus, and m_i, systematically vary with increasing alteration style and pervasiveness, allowing for a clear distinction between fresh and altered rock (Fig. 11g-l), as also shown in (Heap et al. 2021). Porosity, permeability, and Vp have larger data spreads in weathered and altered rock than in fresh rock (Fig. 11a-f), which also reduces systematic trends through alteration type and pervasiveness. Porosity tends

Table 4 Triaxial compressive strength results for varying confining pressures. Blank cells indicate that the confining pressure was not used for a given block

confining → pressure (MPa)	2	3	5	10	15	20	22	25
Block	Peak stress (MPa) for a given confining pressure							
RH2			137	138		231		
RH2b			310	369				
RH4	46	46	73					
RH5			279	292				459
RH6	22	22	35					
RH8			92	131	175			
RH9			163	228			288	
RH10			273	344				479
RH11			178	193				338
RH14			176	201				302
RH15	25	30	65					
RH16			148	239				236
RH17			273	327				536
RH17b			322	495				598
RH19		79	87	147				
RH21			212	273				396
RH22	49	43	55					
RH28	25	45	37					
RH38			128	158		231		
RH42b		61	98	81				
RH50			114	154		200		
RH52			253	230				345
RH52b			82	134	146			
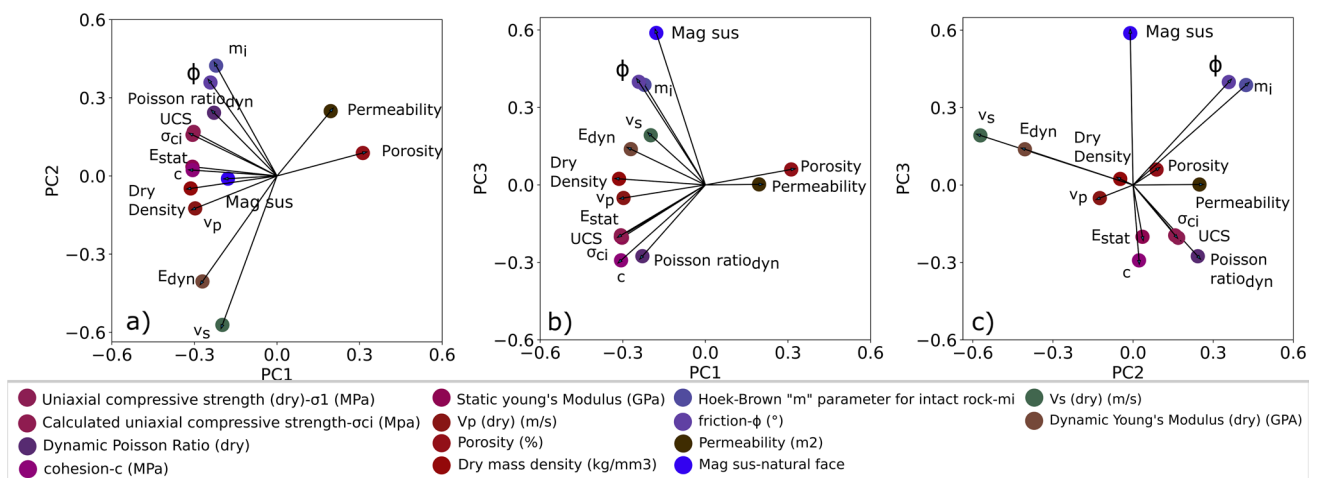
Fig. 10 Biplots of eigenvectors resulting from principal component analysis. Colours are RGB coded according to the x, y and z components of the eigenvectors corresponding to the first three principal components. Similarly coloured parameters have eigenvectors with similar directions in the 3D space defined by the first three principal components

to be higher in altered samples, but more samples in each alteration type and pervasiveness category are required to draw further conclusions (Fig. 11a-b).

Permeability remains within one order of magnitude for all alteration types and pervasiveness, except for supergene and moderate alteration (Fig. 11c-d). Supergene and moderate alteration appear to have a wide range

Fig. 11 Averaged physical and mechanical properties of lava rocks only vs. alteration type and alteration pervasiveness for (**a-b**) porosity, (**c-d**) permeability, (**e–f**) P-wave velocity (Vp), (**g-h**) uniaxial compressive strength (UCS), (**i-j**) static Young's modulus, and (**k-l**) Generalized Hoek–Brown failure criterion intact rock constant m_i. Note that altered specimens (surface weathering, supergene, and steam heated) have various levels of alteration pervasiveness (minor, moderate, pervasive) and therefore different specimens will shift across categories
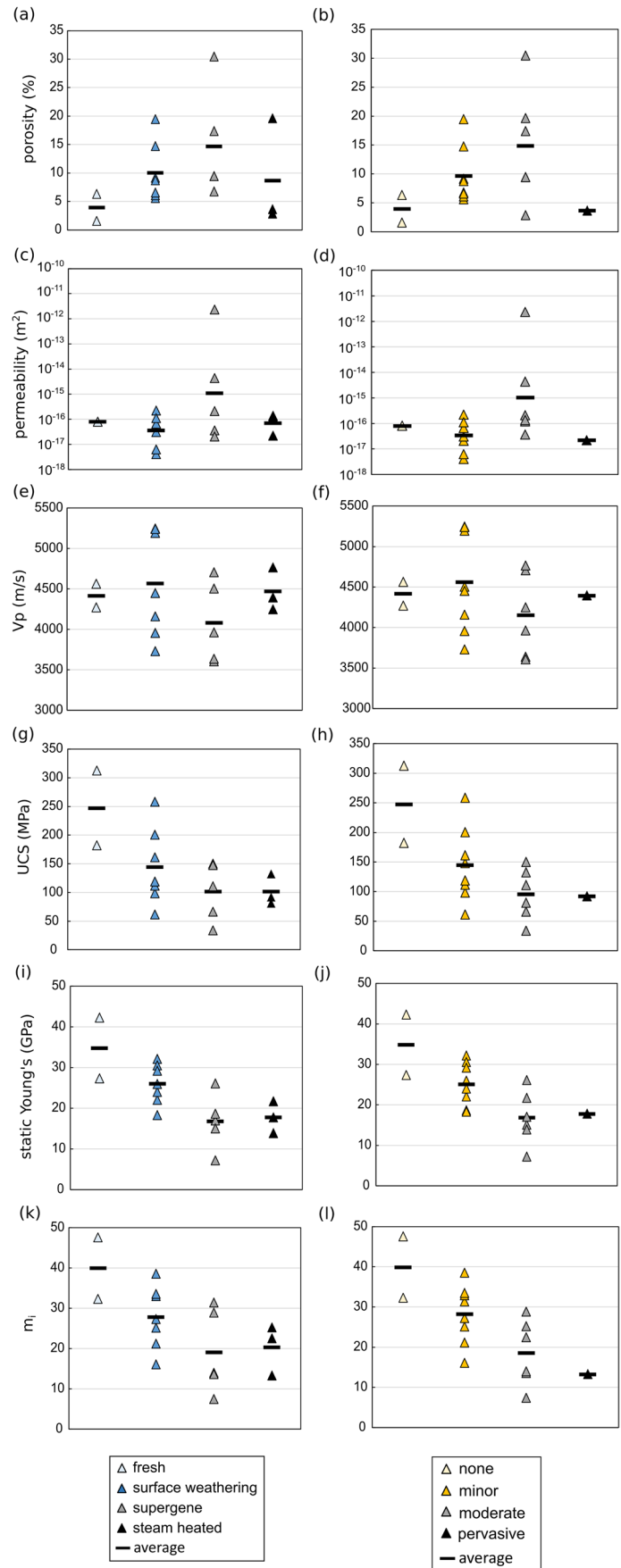
of effects on permeability, although the reason for this is not yet clear due to a small sample number. Additional steam-heated or pervasively altered samples would further clarify the trends seen in this dataset. Pervasively altered samples tend to have the lowest Vp, although a systematic trend through alteration pervasiveness, as observed by other authors such as Pola et al. (2012), is less obvious (Fig. 11e-f).

The relations between physical and mechanical rock properties vary depending on the rock characteristics; for example, porosity may be a better predictor of UCS than alteration type or pervasiveness for rocks with porosity > 10%, whereas alteration and pervasiveness may be better predictors for lavas (which tend to have lower porosity). These trends are affected by high-intensity hydrothermal alteration (Heap et al. 2019b), which develops when rocks are in close proximity to an active hydrothermal system or are exposed to hydrothermal fluid circulation for long periods. This can lead to both primary denser minerals (pyroxene, titanomagnetite) being replaced by less dense secondary minerals (goethite, jarosite), and the precipitation of clay minerals (e.g., kaolinite, montmorillonite) into pores and cracks, resulting in anomalously low porosity, low strength samples (Heap and Violay 2021; Schaefer et al. 2021). This is highlighted by samples RH50 and RH52 (Fig. 6). Sample RH52 is a block of lava taken from the edge of the Crater Lake. The Crater Lake is highly acidic (pH = 0–3) and fluctuates in temperatures (10–60 °C) (Christenson and Wood 1993; Christenson et al. 2010). This sample was subjected to intense alteration and precipitation of clay infilling minerals, particularly in the outer 6 cm, resulting in lower porosity-to-UCS ratios than is typical for lava with low primary porosity (Fig. 4). Sample RH50, a block from the 1995–1996 eruption, represents lava from the upper conduit area within the current vent-hosted hydrothermal system (Kilgour et al. 2010). RH50 has a high percentage of phyllosilicate clay minerals, resulting in anomalously low porosity, low strength, and low magnetic susceptibility (Fig. 4, Fig. 6c, f, i). These anomalous material property relationships are indicative of potentially complex relationships between porosity, mineralogy, and physical and mechanical characteristics of material at depth, which remain to be thoroughly explored.

An additional consideration for material property variations is alteration rate, and spatial and temporal position to aggressive fluids. Alteration by acidic fluids is fairly rapid (Farquharson et al. 2019), and likely faster than surface weathering processes, particularly at high temperatures. For example, samples RH52 and RH42B were both formed in the youngest Whakapapa formation (≤ 15 ky), but RH52 has low porosity yet moderate alteration due to exposure to acidic Crater Lake fluids, while RH42B has high porosity yet remains a fresh sample because it was not exposed to acidic fluids.

Implications for monitoring, modeling, and volcanic hazards

Sample RH50, a lava rock that originated from the upper conduit and was brought to the surface during the 1995–1996 eruptions (see details in Study Area and Materials section), highlights the potential variability of surface from subsurface samples at Ruapehu. The low strength of RH50 due to the high percentage of clay minerals suggests that material in the vent area of Ruapehu (up to 410 m below the Crater Lake; Christenson 2010) could be two times weaker than typical porosity-strength trends of surface samples; RH50 has an average UCS of 93 MPa (Table 3) while the exponential trend suggests a rock with a porosity c. 3.6% would have a UCS c. 190 MPa (Fig. 4). Although we are limited by only having one sample, this does suggest that mechanical properties of the vent area should be carefully considered in numerical modeling. Low apparent magnetic susceptibility (< 0.005 SI), interpreted as a region of altered rock in the current hydrothermal system, has been mapped beneath the Crater Lake extending to ~ 1700 m a.s.l. using an aeromagnetic data inversion (Miller et al. 2020). Other low susceptibility areas have been mapped within the upper cone flanks using a combination of aeromagnetic and hyperspectral surveys and interpreted to be part of older hydrothermal systems (Kereszturi et al. 2020). Thus, larger areas of weak, soft, and altered material may be present throughout Ruapehu's upper flanks than previously expected, or that is obvious from surface observations. This emphasizes the benefit of using ballistic projectiles (fragments of rock expelled during explosive eruptions, such as block RH50) that have originated from the subsurface to measure the properties in currently active hydrothermal systems (Kennedy et al. 2020). However, subsurface volcanic samples useful for mechanical testing are rare, and those that are acquired may require assumptions regarding sample origin and environment. Thus, determining subsurface material properties, especially at meaningful resolution and under realistic laboratory conditions (e.g., varying confining pressures, temperatures, and saturation), remains a challenge.

This dataset additionally emphasizes that, although trends of weathering/alteration and material properties do exist, properties of volcanic rock can vary significantly within each category and within hand-specimen scales. However, fresh material is typically distinguishable from moderately or pervasively altered rock, which suggests that end-member differentiation is possible for physical and mechanical property mapping. The generally strong control of porosity on other physical and mechanical properties suggests that more accurate relations can be made if a dataset is split by lithology (Fig. 4), which typically have distinct porosities due to emplacement mechanisms. The use of different lithology groups will likely result in physical

and mechanical input data at higher spatial resolution than is typically used in geophysical models (Heap et al. 2020).

Implications for spectroscopy-material property correlations

Our data show that, as alteration becomes more prominent, there is a spectral shift from 540 nm to < 450 nm, indicating the occurrence of goethite (430 and 480 nm; Fig. 3a) as a weathering product of hydrothermal pyrite (Kereszturi et al. 2020), and precipitation of native sulfur (390 nm; Fig. 3a). This alteration-induced shift in wavelength location (Fig. 3a) also coincides with alteration-induced changes to material properties (Fig. 11). Using Spearman's ρ statistical value, Schaefer et al. (2021) demonstrate that these tandem shifts result in strong correlations between laboratory reflectance values and rock properties such as magnetic susceptibility, UCS, porosity, density, friction angle, and static Young's modulus. The laboratory spectral signatures of carbonate rocks have also recently been shown to correlate with rock strength (Bakun-Mazor et al. 2021). Given the resource- and time-consuming efforts required to characterize rocks in a laboratory setting, future efforts could explore direct correlations of spectroscopy with physical and mechanical rock properties. Shortwave infrared spectroscopy from remote platforms at volcanoes (e.g., Aslett et al. 2018; Kereszturi et al. 2018; Gabrieli et al. 2019) can further support the spatial interpolation of sparsely sampled material data, resulting in large-scale geotechnical maps.

Conclusion

Physical and mechanical properties were determined for a suite of 23 blocks of andesitic lavas, autoclastic breccias, and pyroclastic rocks from Ruapehu volcano in New Zealand with varying weathering and alteration intensities and mineral assemblages. The large number of samples of lavas and autoclastic breccias allowed the distinction of material relations and systemic changes due to weathering and alteration heterogeneities for these rock types. Expanding this research to include volcanic material from other locations (surface and subsurface) will continue to develop these relationships determined herein. Our key findings are:

(1) Porosity has a dominant effect on many physical and mechanical properties. Lavas typically having lower porosities (< 20%) than autoclastic breccias (> 20 %) and tephra (> 40%).

(2) The type of alteration (i.e., weathering or hydrothermal alteration), including alteration intensity, additionally influences physical and mechanical rock properties. The uniaxial compressive strength, static Young's modulus, and Hoek-Brown constant m_i were found to have more systematic variations with weathering/alteration mineralogy and pervasiveness than variables such as permeability and seismic velocities.

(3) Rocks without weathering or alteration present tend to be less porous and stronger than rock with surface weathering. Rock with surface weathering is less porous, stronger, and less brittle compared to rock with supergene or steam-heated intermediate and advanced argillic weathering.

(4) Vp, density, and Young's modulus show strong relations with material properties such as porosity and strength.

(5) End-member property differentiation is easily distinguishable (e.g., fresh vs. pervasively altered rock). However, rocks with minor to intermediate weathering or alteration tend to have larger variations in properties due to varying consequences of the nature of the host rock, the fluid type and composition, temperature, and the duration of rock-fluid interaction.

(6) Samples near the vent complex do not follow typical porosity-strength trends as surface samples due to the intensity of clay mineral precipitation and replacement. This has implications for varying the brittle-ductile transition zone, preventing fluid flow, and increasing the likelihood of collapse.

Trends in the pervasiveness of weathering with physical and mechanical properties, along with shifts in the position of spectral absorption peaks as hydrothermal/weathering alteration increases, imply it may be possible to correlate intact rock properties to laboratory or imaging spectroscopy measurements. Extrapolating material properties from imaging spectroscopy is a promising avenue of future research, which could be used to facilitate regional-scale mapping of physical and mechanical properties.

Data availability Physical and mechanical results for each specimen, and calculated strength criteria for each block using the Mohr–Coulomb and Generalized Hoek–Brown methods, are available in the Supplementary Material. Additional data are available from the corresponding author upon request.

Declarations

Conflicts of interest The authors have no conflicts of interest to declare that are relevant to the content of this article.

References

Akoglu H (2018) User's guide to correlation coefficients: Turkish. J Emerg Med 18(3):91–93. https://doi.org/10.1016/j.tjem.2018.08.001

Al-Harthi AA, Al-Amri RM, Shehata WM (1999) The porosity and engineering properties of vesicular basalt in Saudi Arabia. Eng Geol 54(3–4):313–320. https://doi.org/10.1016/S0013-7952(99)00050-2

Apuani T, Corazzato C, Cancelli A, Tibaldi A (2005) Stability of a collapsing volcano (Stromboli, Italy): Limit equilibrium analysis and numerical modelling. J Volcanol Geotherm Res 144(1–4):191–210. https://doi.org/10.1016/j.jvolgeores.2004.11.028

Aslett Z, Taranik JV, Riley DN (2018) Mapping rock forming minerals at Boundary Canyon, Death Valley National Park, California, using aerial SEBASS thermal infrared hyperspectral image data. Int J Appl Earth Obs Geoinf 64:326–339. https://doi.org/10.1016/j.jag.2017.08.001

Bakun-Mazor D, Ben-Ari Y, Notesko G, Marco S, Ben-Dor E (2021) Measuring Carbonate Rock Strength using Spectroscopy across the Optical and Thermal Region. In IOP Conf Series Earth Environ Sci, IOP Publishing 833:012025. https://doi.org/10.1088/1755-1315/833/1/012025

Ball JL, Taron J, Reid ME, Hurwitz S, Finn C, Bedrosian P (2018) Combining Multiphase Groundwater Flow and Slope Stability Models to Assess Stratovolcano Flank Collapse in the Cascade Range: Journal of Geophysical Research: Solid. Earth 123(4):2787–2805. https://doi.org/10.1002/2017JB015156

Brace WF, Walsh JB, Frangos WT (1968) Permeability of granite under high pressure. J Geophys Res 73(6):2225–2236. https://doi.org/10.1029/jb073i006p02225

Cai M (2010) Practical estimates of tensile strength and Hoek-Brown strength parameter mi of brittle rocks. Rock Mech Rock Eng 43:167–184. https://doi.org/10.1007/s00603-009-0053-1

Christenson BW (2000) Geochemistry of fluids associated with the 1995–1996 eruption of Mt Ruapehu, New Zealand: Signatures and Processes in the Magmatic-Hydrothermal System. J Volcanol Geotherm Res 97(1–4):1–30. https://doi.org/10.1016/S0377-0273(99)00167-5

Christenson BW, Wood CP (1993) Evolution of a vent-hosted hydrothermal system beneath Ruapehu Crater Lake New Zealand. Bull Volcanol 55:547–565. https://doi.org/10.1007/BF00301808

Christenson BW, Reyes AG, Young R, Moebis A, Sherburn S, Cole-Baker J, Britten K (2010) Cyclic processes and factors leading to phreatic eruption events: Insights from the 25 September 2007 eruption through Ruapehu Crater Lake New Zealand. J Volcanol Geotherm Res 191(1–2):15–32. https://doi.org/10.1016/j.jvolgeores.2010.01.008

Coats R, Kendrick JE, Wallace PA, Miwa T, Hornby AJ, Ashworth JD, Matsushima T, Lavallée Y (2018) Failure criteria for porous dome rocks and lavas: a study of Mt. Unzen, Japan. Solid Earth 9:1299–1328. https://doi.org/10.5281/zenodo.1287237

Conway CE, Leonard GS, Townsend DB, Calvert AT, Wilson CJN, Gamble JA, Eaves SR (2016) A high-resolution 40Ar/39Ar lava chronology and edifice construction history for Ruapehu volcano New Zealand. J Volcanol Geotherm Res 327:152–179. https://doi.org/10.1016/j.jvolgeores.2016.07.006

Crowley JK, Zimbelman DR (1997) Mapping hydrothermally altered rocks on Mount Rainier, Washington, with Airborne Visible/Infrared Imaging Spectrometer (AVIRIS) data. Geology 25(6):559–562. https://doi.org/10.1130/0091-7613(1997)025%3c0559:MHAROM%3e2.3.CO;2

Day SJ (1996) Hydrothermal pore fluid pressure and the stability of porous, permeable volcanoes. Geol Soc London, Spec Publ 110:77–93. https://doi.org/10.1144/GSL.SP.1996.110.01.06

Del Potro R, Hürlimann M (2008) Geotechnical classification and characterisation of materials for stability analyses of large volcanic slopes. Eng Geol 98(1–2):1–17. https://doi.org/10.1016/j.enggeo.2007.11.007

Dobson PF, Kneafsey TJ, Hulen J, Simmons A (2003) Porosity, permeability, and fluid flow in the Yellowstone geothermal system, Wyoming. J Volcanol Geotherm Res 123(3–4):313–324. https://doi.org/10.1016/S0377-0273(03)00039-8

Douglas A, Kereszturi G, Schaefer LN, Kennedy B (2022) Rock alteration mapping in and around fossil shallow intrusions at Mt. Ruapehu New Zealand with laboratory and aerial hyperspectral imaging. J Volcanol Geotherm Res 432:107700. https://doi.org/10.1016/j.jvolgeores.2022.107700

Farquharson JI, Wild B, Kushnir ARL, Heap MJ, Baud P, Kennedy B (2019) Acid-Induced Dissolution of Andesite: Evolution of Permeability and Strength: Journal of Geophysical Research: Solid. Earth 124(1):257–273. https://doi.org/10.1029/2018JB016130

Fernández-Caliani JC, Crespo E, Rodas M, Barrenechea JF, Luque FJ (2004) Formation of nontronite from oxidative dissolution of pyrite disseminated in Precambrian felsic metavolcanics of the Southern Iberian Massif (Spain). Clays and Clay Minerals 52(1):106–114. https://doi.org/10.1346/CCMN.2004.0520110

Fisher RV (1961) Proposed classification of volcaniclastic sediments and rocks. GSA Bull 72(9):1409–1414. https://doi.org/10.1130/0016-7606(1961)72[1409:pcovsa]2.0.co;2

Gonnermann HM, Manga M (2007) The Fluid Mechanics Inside a Volcano. Annu Rev Fluid Mech 39:321–356. https://doi.org/10.1146/annurev.fluid.39.050905.110207

Hackett WR (1985) Geology and petrology of Ruapehu volcano and related vents: PhD dissertation. Victoria University of Wellington

Hackett WR, Houghton BF (1989) A facies model for a quaternary andesitic composite volcano: Ruapehu New Zealand. Bull Volcanol 51:51–68. https://doi.org/10.1007/BF01086761

Heald P, Foley NK, Hayba DO (1987) Comparative anatomy of volcanic-hosted epithermal deposits: acid- sulfate and adularia- sericite types. Econ Geol 82(1):1–26. https://doi.org/10.2113/gsecongeo.82.1.1

Heap MJ, Violay ME (2021) The mechanical behaviour and failure modes of volcanic rocks: a review. Bull Volcanol 83(5):33. https://doi.org/10.1007/s00445-021-01447-2

Heap MJ, Lavallée Y, Petrakova L, Baud P, Reuschle T, Varley NR, Dingwell DB (2014) Microstructural controls on the physical and mechanical properties of edifice-forming andesites at Volcán de Colima, Mexico. J Geophys Res: Solid Earth 119(4):2925–2963. https://doi.org/10.1002/2013JB010521

Heap MJ, Farquharson JI, Wadsworth FB, Kolzenburg S, Russell JK (2015b) Timescales for permeability reduction and strength recovery in densifying magma. Earth Planet Sci Lett 429:223–233. https://doi.org/10.1016/j.epsl.2015.07.053

Heap MJ, Kennedy BM, Pernin N, Jacquemard L, Baud P, Farquharson JI, Scheu B, Lavallée Y, Gilg HA, Letham-Brake M (2015c) Mechanical behaviour and failure modes in the Whakaari (White Island

volcano) hydrothermal system New Zealand. J Volcanol Geotherm Res 295:26–42. https://doi.org/10.1016/j.jvolgeores.2015.02.012

Heap MJ, Gravley DM, Kennedy BM, Gilg HA, Bertolett E, Barker SLL (2019) Quantifying the role of hydrothermal alteration in creating geothermal and epithermal mineral resources: The Ohakuri ignimbrite (Taupo Volcanic Zone, New Zealand). J Volcanol Geotherm Res 390:106703. https://doi.org/10.1016/j.jvolgeores.2019.106703

Heap MJ, Villeneuve M, Albino F, Farquharson JI, Brothelande E, Amelung F, Got JL, Baud P (2020) Towards more realistic values of elastic moduli for volcano modelling. J Volcanol Geotherm Res 360:106684. https://doi.org/10.1016/j.jvolgeores.2019.106684

Heap MJ, Baumann TS, Rosas-Carbajal M, Komorowski JC, Gilg HA, Villeneuve M, Moretti R, Baud P, Carbillet L, Harnett C, Reuschlé T (2021) Alteration-Induced Volcano Instability at La Soufrière de Guadeloupe (Eastern Caribbean). J Geophys Res: Solid Earth 126(8):e2021JB022514. https://doi.org/10.1029/2021JB022514

Henkel H (1994) Standard diagrams of magnetic properties and density—a tool for understanding magnetic petrology. J Appl Geophys 32(1):43–53. https://doi.org/10.1016/0926-9851(94)90008-6

Hickey J, Lloyd R, Biggs J, Arnold D, Mothes P, Muller C (2020) Rapid localized flank inflation and implications for potential slope instability at Tungurahua volcano Ecuador. Earth Planet Sci Lett 534:116104. https://doi.org/10.1016/j.epsl.2020.116104

Hoek E, Brown ET (1980) Empirical strength criterion for rock masses. J Geotech Eng 106(9):1013–1035. https://doi.org/10.1061/AJGEB6.0001029

Hoek E, Brown ET (1997) Practical estimates of rock mass strength. Int J Rock Mech Min 34(8):1165–1186. https://doi.org/10.1016/S1365-1609(97)80069-X

Huang Z, Turner BJ, Dury SJ, Wallis IR, Foley WJ (2004) Estimating foliage nitrogen concentration from HYMAP data using continuum removal analysis. Remote Sens Environ 93(1–2):18–29. https://doi.org/10.1016/j.rse.2004.06.008

Hunt GR, Ashley RP (1979) Spectra of altered rocks in the visible and near infrared. Econ Geol 74(7):1613–1629. https://doi.org/10.2113/gsecongeo.74.7.1613

Kereszturi G, Schaefer LN, Schleiffarth WK, Procter J, Pullanagari RR, Mead S, Kennedy B (2018) Integrating airborne hyperspectral imagery and LiDAR for volcano mapping and monitoring through image classification. Int J Appl Earth Obs Geoinf 73:323–339. https://doi.org/10.1016/j.jag.2018.07.006

Kereszturi G, Schaefer LN, Miller C, Mead S (2020) Hydrothermal Alteration on Composite Volcanoes -Mineralogy, Hyperspectral Imaging and Aeromagnetic Study of Mt Ruapehu, New Zealand. Geochem, Geophys, Geosyst 21(9):e2020GC009270. https://doi.org/10.1029/2020GC009270

Kilgour G, Manville V, Pasqua F, Della AG, Hodgson KA, Jolly GE (2010) The 25 September 2007 eruption of Mount Ruapehu New Zealand: Directed Ballistics, Surtseyan Jets, and Ice-Slurry Lahars. J Volcanol Geotherm Res 191(1–2):1–14. https://doi.org/10.1016/j.jvolgeores.2009.10.015

Kokaly RF, Clark RN (1999) Spectroscopic Determination of Leaf Biochemistry Using Band-Depth Analysis of Absorption Features and Stepwise Multiple Linear Regression. Remote Sens Environ 67(3):267–287. https://doi.org/10.1016/S0034-4257(98)00084-4

López DL, Williams SN (1993) Catastrophic volcanic collapse: Relation to hydrothermal processes. Science 260(5115):1794–1796. https://doi.org/10.1126/science.260.5115.1794

Miller C, Schaefer LN, Kereszturi G, Fournier D (2020) Three dimensional mapping of Mt Ruapehu volcano, New Zealand, from aeromagnetic data inversion and hyperspectral imaging. J Geophys Res: Solid Earth 125(2):e2019JB018247. https://doi.org/10.1029/2019JB018247

Mordensky SP, Villeneuve MC, Kennedy BM, Heap MJ, Gravley DM, Farquharson JI, Reuschlé T (2018) Physical and mechanical

property relationships of a shallow intrusion and volcanic host rock, Pinnacle Ridge, Mt Ruapehu, New Zealand. J Volcanol Geotherm Res 359:1–20. https://doi.org/10.1016/j.jvolgeores.2018.05.020

Mordensky SP, Kennedy BM, Villeneuve MC, Lavallée Y, Reichow MK, Wallace PA, Siratovich PA, Gravley DM (2019b) Increasing the Permeability of Hydrothermally Altered Andesite by Transitory Heating. Geochem Geophys, Geosyst 20(11):5251–5269. https://doi.org/10.1029/2019GC008409

Mordensky SP, Villeneuve MC, Kennedy BM, Struthers J, Gravley DM (2022) Mechanical rock mass behaviour surrounding a shallow intrusion in andesitic lavas at Pinnacle Ridge, Mt. Ruapehu (New Zealand): pore-pressure induced edifice destabilization. Eng Geol 305:106696. https://doi.org/10.1016/j.enggeo.2022.106696

Nakagawa M, Wada K, Thordarson T, Wood CP, Gamble JA (1999) Petrologic investigations of the 1995 and 1996 eruptions of Ruapehu volcano New Zealand: Formation of discrete and small magma pockets and their intermittent discharge. Bull Volcanol 61:15–31. https://doi.org/10.1007/s004450050259

Neal LC, Wilkinson JJ, Mason PJ, Chang Z (2018) Spectral characteristics of propylitic alteration minerals as a vectoring tool for porphyry copper deposits. J Geochem Explor 184:179–198. https://doi.org/10.1016/j.gexplo.2017.10.019

Pola A, Crosta G, Fusi N, Barberini V, Norini G (2012) Influence of alteration on physical properties of volcanic rocks. Tectonophysics 566–567:67–86. https://doi.org/10.1016/j.tecto.2012.07.017

Price RC, Gamble JA, Smith IEM, Maas R, Waight T, Stewart RB, Woodhead J (2012) The anatomy of an andesite volcano: A time-stratigraphic study of andesite petrogenesis and crustal evolution at Ruapehu Volcano New Zealand. J Petrol 53(10):2139–2189. https://doi.org/10.1093/petrology/egs050

Reid ME, Sisson TW, Brien DL (2001) Volcano collapse promoted by hydrothermal alteration and edifice shape Mount Rainier, Washington. Geology 29(9):779–782. https://doi.org/10.1130/0091-7613(2001)029%3c0779:VCPBHA%3e2.0.CO;2

Rye RO (2005) A review of the stable-isotope geochemistry of sulfate minerals in selected igneous environments and related hydrothermal systems. Chem Geol 215(1–4):5–36. https://doi.org/10.1016/j.chemgeo.2004.06.034

Saubin E, Kennedy B, Tuffen H, Villeneuve M, Davidson J, Burchardt S (2019) Comparative field study of shallow rhyolite intrusions in Iceland: Emplacement mechanisms and impact on country rocks. J Volcanol Geotherm Res 388:106691. https://doi.org/10.1016/j.jvolgeores.2019.106691

Schaefer LN, Oommen T, Corazzato C, Tibaldi A, Escobar-Wolf R, Rose WI (2013) An integrated field-numerical approach to assess slope stability hazards at volcanoes: the example of Pacaya, Guatemala. Bull Volcanol 75:1–18. https://doi.org/10.1007/s00445-013-0720-7

Schaefer LN, Kendrick JE, Lavallée Y, Oommen T, Chigna G (2015) Geomechanical rock properties of a basaltic volcano. Front Earth Sci 3:29. https://doi.org/10.3389/feart.2015.00029

Schaefer LN, Kereszturi G, Villeneuve M, Kennedy B (2021) Determining physical and mechanical volcanic rock properties via reflectance spectroscopy. J Volcanol Geotherm Res 420:107393. https://doi.org/10.1016/j.jvolgeores.2021.107393

Schwertmann U, Murad E (1983) Effect of pH on the formation of goethite and hematite from ferrihydrite. Clays Clay Miner 31:277–284. https://doi.org/10.1346/CCMN.1983.0310405

Severin KP (2004) Energy dispersive spectrometry of common rock forming minerals: Dordrecht. Kluwer Academic, The Netherlands. https://doi.org/10.1007/978-1-4020-2841-0

Siratovich PA, Heap MJ, Villeneuve MC, Cole JW, Kennedy BM, Davidson J, Reuschlé T (2016) Mechanical behaviour of the Rotokawa Andesites (New Zealand): Insight into permeability evolution and stress-induced behaviour in an actively utilised

geothermal reservoir. Geothermics 64:163–179. https://doi.org/10.1016/j.geothermics.2016.05.005

Swayze GA, Clark RN, Goetz AF, Livo KE, Breit GN, Kruse FA, Sutley SJ, Snee LW, Lowers HA, Post JL, Stoffregen RE (2014) Mapping advanced argillic alteration at Cuprite, Nevada, using imaging spectroscopy. Econ Geol 109(5):1179–1221. https://doi.org/10.2113/econgeo.109.5.1179

van der Meer F (2018) Near-infrared laboratory spectroscopy of mineral chemistry: A review. Int J Appl Earth Obs Geoinf 65:71–78. https://doi.org/10.1016/j.jag.2017.10.004

van Ruitenbeek FJA, van der Werff HMA, Bakker WH, van der Meer FD, Hein KAA (2019) Measuring rock microstructure in hyperspectral mineral maps. Remote Sens Environ 220:94–109. https://doi.org/10.1016/j.rse.2018.10.030

Vanorio T, Prasad M, Patella D, Nur A (2002) Ultrasonic velocity measurements in volcanic rocks: Correlation with microtexture. Geophys J Int 149(1):22–36. https://doi.org/10.1046/j.0956-540x.2001.01580.x

Wallace CS, Schaefer LN, Villeneuve MC (2021) Material Properties and Triggering Mechanisms of an Andesitic Lava Dome Collapse at Shiveluch Volcano Kamchatka, Russia, Revealed Using the Finite Element Method. Rock Mech Rock Eng 55:2711–2728. https://doi.org/10.1007/s00603-021-02513-z

Watters RJ, Zimbelman DR, Bowman SD, Crowley JK (2000) Rock mass strength assessment and significance to edifice stability, Mount Rainier and Mount Hood, Cascade Range volcanoes. Pure Appl Geophys 157:957–976. https://doi.org/10.1007/s000240050012

White JDL, Houghton BF (2006) Primary Volcaniclastic Rocks. Geology 34(8):677–680. https://doi.org/10.1130/G22346.1

Wong TF, Baud P (2012) The brittle-ductile transition in porous rock: A review. J Struct Geol 44:25–53. https://doi.org/10.1016/j.jsg.2012.07.010

Wyering LD, Villeneuve MC, Wallis IC, Siratovich PA, Kennedy BM, Gravley DM, Cant JL (2014) Mechanical and physical properties of hydrothermally altered rocks, Taupo Volcanic Zone, New Zealand. J Volcanol Geoth Res 288:76–93. https://doi.org/10.1016/j.jvolgeores.2014.10.008

Yildiz A, Kuşcu M, Dumlupunar I, Ekrem ArItan A, BağcI M (2010) The determination of the mineralogical alteration index and the investigation of the efficiency of the hydrothermal alteration on physico-mechanical properties in volcanic rocks from Köprülü Afyonkarahisar, West Turkey. Bull Eng Geol Environ 65:51–61. https://doi.org/10.1007/s10064-009-0245-7

Zimbelman DR, Rye RO, Breit GN (2005) Origin of secondary sulfate minerals on active andesitic stratovolcanoes. Chem Geol 215(1–4):37–60. https://doi.org/10.1016/j.chemgeo.2004.06.056

Ball JL, Calder ES, Hubbard BE, Bernstein ML (2013) An assessment of hydrothermal alteration in the Santiaguito lava dome complex, Guatemala: Implications for dome collapse hazards: Bull Volcanol 75(676). https://doi.org/10.1007/s00445-012-0676-z

Cant JL, Siratovich PA, Cole JW, Villeneuve MC, Kennedy BM (2018) Matrix permeability of reservoir rocks, Ngatamariki geothermal field, Taupo Volcanic Zone, New Zealand: Geotherm Energy, 6(2). https://doi.org/10.1186/s40517-017-0088-6

Carter T (2020) A suggested visual approach for estimating Hoek-Brown mi for different rock types, In Conference: ISRM Congress: Rock Mechanics for Natural Resources and Infrastructure Development, Foz do Iguassu, Brazil, ISBN: 978–0–367–42284–4

Clark R (1999) Spectroscopy of rocks and minerals, and principles of spectroscopy: In: Remote Sensing for the Earth Sciences: Manual of Remote Sensing, 3(11) 3–58. ISBN: 0471–29405–5

Danner M, Locherer M, Hank T, Richter K (2015) Spectral Sampling with the ASD FIELDSPEC 4: EnMAP Field Guides Technical Reports, EnMAP Hyperspectral Imager: 1–20.

Frolova JV, Gvozdeva IP, Kuznetsov NP (2015) Effects of Hydrothermal Alterations on Physical and Mechanical Properties of Rocks

in the Geysers Valley (Kamchatka Peninsula) in Connection with Landslide Development: World Geothermal Congress 2015.

Gabrieli A, Wright R, Porter JN, Lucey PG, Honnibal C (2019) Applications of quantitative thermal infrared hyperspectral imaging (8–14 µm): measuring volcanic SO2 mass flux and determining plume transport velocity using a single sensor. Bull Volcanol: 81(47). https://doi.org/10.1007/s00445-019-1305-x

Guéguen Y, Palciauskas V (1994) Introduction to the Physics of Rocks: Princeton University Press. ISBN 0–691–03452–4

Heap MJ, Xu T, Chen CF (2014b) The influence of porosity and vesicle size on the brittle strength of volcanic rocks and magma. Bull Volcanol 76 (856) https://doi.org/10.1007/s00445-014-0856-0

Heap MJ, Farquharson JI, Baud P, Lavallée Y, Reuschlé T (2015a) Fracture and compaction of andesite in a volcanic edifice: Bull Volcanol 77(55). https://doi.org/10.1007/s00445-015-0938-7

Heap MJ, Troll VR, Kushnir ARL, Gilg HA, Collinson ASD, Deegan FM, Darmawan H, Seraphine N, Neuberg J, Walter TR, (2019b) Hydrothermal alteration of andesitic lava domes can lead to explosive volcanic behaviour. Nat Commun 10 (5063) https://doi.org/10.1038/s41467-019-13102-8

Hill, S., 2020, Mechanical rock property characterisation and assessment of sandstone reservoirs in the Southern Taranaki Basin: PhD Thesis, University of Canterbury.

Jolliffe I (2005) Principal component analysis: Encyclopedia of statistics in behavioral science. John Wiley and Sons Ltd, New York, p. 1580 -1584. https://doi.org/10.1002/0470013192.bsa501

Kennedy BM, Farquhar A, Hilderman R, Villeneuve MC, Heap MJ, Mordensky S, Kilgour G, Jolly A, Christenson B, Reuschlé, T (2020) Pressure controlled permeability in a conduit filled with fractured hydrothermal Breccia reconstructed from ballistics from Whakaari (White island), New Zealand. Geosciences, 10(4). https://doi.org/10.3390/geosciences10040138

Labuz JF, Zang A (2012) Mohr–Coulomb failure criterion, in The ISRM Suggested Methods for Rock Characterization, Testing and Monitoring: 2007–2014, Springer 227–231.

Lu Z, Masterlark T, Dzurisin D (2005) Interferometric synthetic aperture radar study of Okmok volcano, Alaska, 1992–2003: Magma supply dynamics and postemplacement lava flow deformation. J Geophys Res: Solid Earth (1978–2012), 110(B2). https://doi.org/10.1029/2004JB003148

Mordensky SP, Heap MJ, Kennedy BM, Gilg HA, Villeneuve MC, Farquharson JI, Gravley DM (2019a) Influence of alteration on the mechanical behaviour and failure mode of andesite: implications for shallow seismicity and volcano monitoring. Bull Volcanol 81(44). https://doi.org/10.1007/s00445-019-1306-9

Okada N, Maekawa Y, Owada N, Haga K, Shibayama A, Kawamura Y (2020) Automated Identification of Mineral Types and Grain Size Using Hyperspectral Imaging and Deep Learning for Mineral Processing. Minerals 10 (9) https://doi.org/10.3390/min10090809

Richards LR, Read SAL (2011) A comparison of methods for determining mi, the Hoek-Brown parameter for intact rock material: 45th US Rock Mechanics / Geomechanics Symposium.

Scott BJ (2013) A revised catalogue of Ruapehu volcano eruptive activity: 1830–2012: GNS Science Open Report.

Shindo D, Oikawa T (2002) Energy dispersive x-ray spectroscopy: In: Analytical electron microscopy for materials science, Springer, Tokyo: 81–102. https://doi.org/10.1007/978-4-431-66988-3_4

Simmons SF, White NC, John DA (2005) Geological characteristics of epithermal precious and base metal deposits: Economic Geology; One hundredth anniversary volume, 1905–2005. https://doi.org/10.5382/AV100.16

Siratovich PA, Heap MJ, Villeneuve MC, Cole JW, Reuschlé T (2014) Physical property relationships of the Rotokawa Andesite, a significant geothermal reservoir rock in the Taupo Volcanic Zone, New Zealand. Geotherm Energy 2 (10) https://doi.org/10.1186/s40517-014-0010-4

Townsend D, Leonard G, Conway C, Eaves S, Wilson C (2017) Geology of the Tongariro National Park Area 1:60 000: Lower Hutt, New Zealand, New Zealand, GNS Science.

Vilhelm J, Ivankina T, Lokajíček, Rudajev V (2016) Comparison of laboratory and field measurements of P and S wave velocities of a peridotite rock. Int J Rock Mech Mining Sci 88235–241 https://doi.org/10.1016/j.ijrmms.2016.07.027

Villeneuve MC, Heap MJ (2021) Calculating the cohesion and internal friction angle of volcanic rocks and rock masses. Volcanica 4(2) https://doi.org/10.30909/vol.04.02.279293

Villeneuve M, Kennedy B, Gravley D, Mordensky SP, Heap MJ, Siratovich P, Wyering L, Cant J (2020) Characteristics of altered volcanic rocks in geothermal reservoirs: In: ISRM Congress: Rock Mechanics for Natural Resources and Infrastructure Development, Foz do Iguassu, Brazil, ISBN: 978–0–367–42284–4

Villeneuve M, Heap MJ, Schaefer LN (2021) Defining the Hoek-Brown Constant mi for Volcanic Lithologies: In: Rock Mechanics and Engineering Geology in Volcanic Fields, CRC Press, 261–268.